A Numerical Study of Linear Inversion in Layered Viscoacoustic Media

Joakim O. Blanch

The Rice Inversion Project, Department of Geology and Geophysics, Rice University, Houston TX 77251-1892

William W. Symes

The Rice Inversion Project, Department of Computational and Applied Mathematics, Rice University, Houston TX 77251-1892

ABSTRACT

Real Earth media attenuate and disperse propagating waves. Viscoelasticity provides an appropriate and powerful tool to model these anelastic effects, so forms a plausible basis for inversion algorithms. The τ-p (intercept time-slowness) domain permits economical modeling and inversion of 3-D wave propagation in layered media, hence provides an appropriate arena for a preliminary synthetic study of anelastic inversion. The adjoint state method leads to an efficient algorithm for linear least squares inversion of short wavelength model components.

Numerical experiments show that accurate and efficient linearized inversion requires: 1) attenuation and dispersion modeling with some accuracy; 2) careful interpretation of inversion results to distinguish between band limitation and other artifacts from signal; 3) conditioning of the data by a time varying gain, hence also of the simulator output, to "equalize" the influence of earlier strong events and later attenuated events. In particular neglect of attenuation severely damages inference

of parameter relationships. Thus reliable AVO analysis must take attenuation into account.

INTRODUCTION

Propagating waves are dispersed and attenuated in real media. Results from AVO analysis are naturally affected by such attenuation (Martinez, 1993; Samec and Blangy, 1992). The "AVO data set" (Keys and Foster, 1995), provided by Mobil, was collected in an attenuating environment, as is clear from the accompanying logs. Q_P is on the average somewhere around 100 for all depths. To effectively understand and interpret the AVO response in reflection data, it is necessary to understand the quantitative effects of attenuation and dispersion on AVO. However since many current methods of AVO interpretation either neglect attenuation of waves or compensate only roughly for attenuation.

The basis for our investigation is an inversion algorithm for layered viscoacoustic media in the $\tau - p$ (intercept time - slowness) domain. We chose to work in the $\tau - p$ domain, since for layered models at least modeling and inversion in the $\tau - p$ domain is computationally relatively inexpensive.

We will confound "AVO processing" with "estimation of short scale fluctuations in several mechanical parameters". In fact, typical AVO attributes such as slope and intercept originate on combinations of elastic parameters in simple models of elastic wave reflection, see for example Shuey (1985).

Viscoelasticity provides a good model for representing real earth media (Blanch et al., 1993a). Attenuation of propagating waves is often measured by the quality factor Q. Sedimentary rocks have been shown to have a nearly constant Q over the seismic frequency range. A simple viscoelastic model using standard linear solids in parallel can closely approximate this behavior, (Blanch et al., 1995), (Blanch et al., 1993a), (Bourbie et al., 1987). In many applications a single standard linear solid suffices, (Blanch et al., 1995), (Blanch et al., 1993a). We have developed a reliable simulator which solves the viscoelastic wave equation using the finite difference method. The forward simulator has already been used in 2-D and 3-D scattering studies and been subject to several convergence tests, (Blanch et al., 1993b), (Robertsson et al., 1993).

To simplify the modeling and inversion tasks, we choose viscoacoustics rather than viscoelasticity as the framework for our experiments. Thus density and velocity (or bulk modulus) fluctuations are the product of the inversion. Proper account of actual physical AVO effects would require viscoelastic modeling; use of the technique presented here with field data would present a combination of elastic parameter fluctuations as a putative density fluctuation.

The inversion algorithm derived here is similar to an algorithm of Martinez and McMechan, (Martinez and McMechan, 1991). Both algorithms use plane wave data and a layered model. Martinez and McMechan's algorithm uses propagator matrices to model the wave field, hence is intrinsically limited to layered models. Our time domain simulator in contrast is a member of a family which includes 2 and 3D simulators (Robertsson et al., 1994a). We have developed an efficient 2D linearized inversion algorithm based on the 2D (line source) simulator. Application of this inversion algorithm to a small part of the Mobil AVO data set was presented at the SEG workshop (Keys and Foster, 1995).

We will start by briefly discussing the simulator and its modification for plane wave layered media simulations. We will then use this simulator to derive a least squares inversion algorithm for plane wave data and layered media, through the adjoint state technique. Finally, a suite of numerical experiments will address properties of and difficulties with inversion in viscoelastic media, such as: (i) Resolution ability in viscoelastic media. (ii) Necessity of accounting for $Q < \infty$, to accurately estimate other material properties. (iii) Conditioning of the data by a time varying gain, hence also of the simulator output, to "equalize" the influence of earlier strong events and later attenuated events, and so yield accurate and efficient inversions.

In particular, we will illustrate some interpretational pitfalls, which may result from neglect of attenuation and dispersion. While our examples are very simple, we believe that they point to typical, rather than special, effects.

FORWARD MODELING

The three dimensional viscoacoustic wave equation for one standard linear solid can be written (Blanch et al., 1993a), (Robertsson et al., 1994a),

$$\left\{ \begin{array}{l} p_{,t} = -K(1+\tau)\nabla \cdot \vec{v} - r + f(\vec{x}_s, t) \\ \\ r_{,t} = -\dfrac{1}{\tau_\sigma}(r + K\tau\nabla \cdot \vec{v}) \\ \\ \vec{v}_{,t} = -\dfrac{1}{\rho}\nabla p \end{array} \right. , \tag{1}$$

which is an initial value problem, i.e., $p = r = 0$, $\vec{v} = \vec{0}$, $t \ll 0$. K is the bulk modulus, ρ is the density and τ is roughly proportional to the inverse of Q and a measure of attenuation, (Blanch et al., 1995). τ_σ is a relaxation time and determines the frequency range where there is most attenuation. p is the pressure (stress) and $\vec{v} = (v_x, v_y, v_z)$ is the particle velocity. r is called a memory variable, which reflects the 'memory' of the viscoelastic medium. Waves are initiated by sources, $f(\vec{x}_s, t)$, which are added to the right hand side of equation (1). The field p is sampled at receiver locations, $\vec{x}_r$, to produce a pressure seismogram, $p(\vec{x}_s, \vec{x}_r, t)$.

Assuming a layered model, $K = K(z)$, $\rho = \rho(z)$, $\tau = \tau(z)$, it is possible to Radon transform equation (1) to the τ-p_s domain. The result is a 1-D wave equation with a modified bulk modulus.

$$
\begin{cases}
p_{,t} = -K_{mod}(1+\tau)v_{,z} - r + f(z_s,t) \\
\\
r_{,t} = -\dfrac{1}{\tau_\sigma}(r + K_{mod}\,\tau v_{,z}) \\
\\
v_{,t} = -\dfrac{1}{\rho}p_{,z}
\end{cases}
\quad , \tag{2}
$$

where

$$
K_{mod} = \frac{K}{1 - p_s^2 K/\rho}, \tag{3}
$$

$v = v_z$, and p_s is the horizontal slowness. The solutions to this transformed wave equation are plane waves with normals (Poynting-vectors) in the x-z plane. The simulated seismogram is defined as $F(\vec{\mu}, t, p_s) = p(z_r, t, p_s)$.

The formula for scaling of the bulk modulus was derived using a non-viscous wave equation, which results in a small approximation for the viscoelastic case, attenuation is underestimated for large slowness values. Equation (2) was solved with the finite difference method. The finite difference solver uses a staggered scheme, which is second order accurate in time and fourth order accurate in space. p and v are updated in time by the leap-frog scheme and r by Crank-Nicolson, (Robertsson et al., 1994a).

LINEARIZED INVERSION

The object of seismic inversion is to find an earth model, $\vec{\mu} = (K, \rho, \tau)$, which yields the best fit between the simulated seismogram, $F(\vec{\mu})$, and the measured seismogram, F_0^{obs}. Measuring the fit with the L^2 norm leads to minimizing the following functional J,

$$
\begin{aligned}
J &= \frac{1}{2}(F(\vec{\mu}) - F_0^{obs}, F(\vec{\mu}) - F_0^{obs}) \\
&\equiv \frac{1}{2}\int\int (F(\vec{\mu}) - F_0^{obs})^2 \, dt dp_s.
\end{aligned} \tag{4}
$$

$F(\vec{\mu})$ is clearly a nonlinear function of the parameters $\vec{\mu}$. Assuming there exists a reasonably good estimate, $\vec{\mu}_0$, it is justified to linearize $F(\vec{\mu})$ to get a linearized map $DF(\delta\vec{\mu})$ and use it instead of F in the functional J, $\vec{\mu} = \vec{\mu}_0 + \delta\vec{\mu}$. It is of course also necessary to change F_0^{obs} to $F^{obs} = F_0^{obs} - F(\vec{\mu}_0)$. This yields,

$$J = \frac{1}{2}(DF[\delta\vec{\mu}] - F^{obs}, DF[\delta\vec{\mu}] - F^{obs}), \tag{5}$$

where square brackets are used to emphasize that $DF[\delta\vec{\mu}]$ is linear in $\delta\vec{\mu}$. Since J is a positive semi-definite form it will have a minimum when a perfect fit occurs. The gradient of J with respect to $\delta\vec{\mu}$ will therefore vanish at this point. A small variation of dJ yields,

$$dJ = (DF[d\delta\vec{\mu}], DF[\delta\vec{\mu}] - F^{obs}), \tag{6}$$

since DF is linear. $d\delta\vec{\mu}$ is a variation of $\delta\vec{\mu}$. By introducing the adjoint DF^* of DF, it is possible to rewrite equation (6) as,

$$dJ = (d\delta\vec{\mu}, DF^*[DF[\delta\vec{\mu}] - F^{obs}]), \tag{7}$$

Now it is possible, through Riez' representation theorem, to identify the gradient of J with respect to $\delta\vec{\mu}$ as,

$$Grad\, J = DF^*[DF[\delta\vec{\mu}] - F^{obs}]. \tag{8}$$

Setting this gradient to zero yields the normal equations,

$$DF^*[DF[\delta\vec{\mu}]] = DF^*[F^{obs}]. \tag{9}$$

Solving equation (9) yields the $\delta\vec{\mu}_{est}$ that minimizes J.

$$\delta\vec{\mu}_{est} = (DF^*DF)^{-1}DF^*[F^{obs}] \tag{10}$$

To utilize the formula in equation (9) it is necessary to derive the linearized forward map DF, by perturbing the parameters determining the media (K, ρ, τ) and the fields describing the viscoelastic waves (p, v, r). The linear terms in the perturbations are kept to produce the linearized forward map.

$$\left\{\begin{array}{l} \delta p_{,t} = -K_{mod}(1+\tau)\delta v_{,z} - \delta r - [\delta K_{mod}(1+\tau) + K_{mod}\delta\tau]v_{,z} \\ \\ \delta r_{,t} = -\dfrac{1}{\tau_\sigma}\left(\delta r + K_{mod}\,\tau\delta v_{,z} + [\delta K_{mod}\,\tau + K_{mod}\,\delta\tau]v_{,z}\right) \\ \\ \delta v_{,t} = -\dfrac{1}{\rho}\delta p_{,z} + \dfrac{\delta\rho}{\rho^2}p_{,z} \end{array}\right. , \tag{11}$$

where $\delta p(z_r, t)$ is sampled at locations x_r to produce a linearized seismogram. Due to the scaling of K in equation (3) the linearized bulk modulus is,

$$\delta K_{mod} = \delta K\left(1 + \frac{K_{mod}}{\rho}p_s^2\right)^2 - \delta\rho\left(\frac{K_{mod}^2}{\rho^2}p_s^2\right). \tag{12}$$

This linearized forward map is identical to a Born approximation.

The adjoint DF^* of DF is found through the adjoint state technique, (Lion, 1971), (Tarantola, 1988). This involves solving a final value equation system, which is the adjoint of the linearized equation (11).

$$\left\{\begin{array}{l} u_{,t} = -\left(\dfrac{1}{\rho}q\right)_{,z} - q0 \\ \\ s_{,t} = \dfrac{1}{\tau_\sigma}(s+u) \\ \\ q_{,t} = -\left(K_{mod}(1+\tau)u - K_{mod}\tau s\right)_{,z} \end{array}\right. \tag{13}$$

$u = q = s = 0$, $t \gg 0$. q, u, and s are the adjoint fields. The source, $q0(z_r, t, p_s)$, in equation (13) is either a residual seismogram, i.e., F^{obs}, or output from the linearized forward map, $F[\vec{\mu}]$. As a matter of fact it can be any "seismogram-like" object. The adjoint fields are used to find the adjoint for the modified parameters by cross correlating the adjoint fields in equation (13) with the background fields, equation (2),

$$\begin{cases} \delta K_{mod-est} = \int_0^T -(1+\tau)v_{,z}u - \tau v_{,z}s \; dt \\ \delta \tau_{mod-est} = \int_0^T -K_{mod}v_{,z}u - K_{mod}v_{,z}s \; dt \\ \delta \rho_{mod-est} = \int_0^T \frac{1}{\rho^2}p_{,z}q \; dt \end{cases} \tag{14}$$

As a final step to find the full adjoint DF^* it is necessary to find the adjoint of the operator modifying the linearized bulk modulus in equation (12). This adjoint modifies the preliminary estimated density and bulk modulus;

$$\begin{cases} \delta K_{est} = \delta K_{mod-est}\left(1 + \frac{K_{mod}}{\rho}p_s^2\right)^2 \\ \delta \tau_{est} = \delta \tau_{mod-est} \\ \delta \rho_{est} = \delta \rho_{mod-est} - \delta K_{mod-est}\frac{K_{mod}^2}{\rho^2}p_s^2 \end{cases} . \tag{15}$$

$(\delta K_{est}, \delta \rho_{est}, \delta \tau_{est})$ in equation (15) is the final adjoint output. It is necessary to derive the adjoint DF^* using the discretized system to find the correct discrete adjoint DF^*. It is clear from the above derivation that the linearized forward map DF and its adjoint DF^* do not exist explicitly. Therefore, it is necessary to use an iterative method to solve the normal equation (9), and since the operator DF^*DF clearly is positive semi-definite it is possible to use the conjugate gradient or residual method to find the solution of the inverse problem $\delta \vec{\mu}_{est}$.

SHORT INVESTIGATION OF VISCOACOUSTIC INVERSION

An inversion algorithm is not useful unless some properties about it are known. This section will address properties of the algorithm and of inversion in viscous media in general. Some initial result will be derived in and analyzed for 1D media. More complicated issues such as multiparameter inversion, which needs a range of offsets to work, will be analyzed with layered media inversion.

Elastic versus Viscoelastic Inversion

The first intriguing investigation would naturally be to invert the same seismogram with an elastic and a viscoelastic reference model. The seismogram should be produced with viscoelastic modeling to make it as realistic as possible. The experiment would give a hint into how important viscous effects are for correct inversion results. This initial experiment is performed in a constant velocity, density and attenuation 1D medium, since it is far more easy to analyze the results in such a simple setting.

We produced a synthetic 1-D seismogram by using a single value for the slowness, p_s. The synthetic model consisted of one distinct reflector, Figure 1 (perturbation in bulk-modulus), the velocity and density were constant $2.0\,km/s$ and $2.6\,g/cm^3$ respectively throughout the model, and Q was approximately 40. We used this seismogram as input to our inversion routine and performed viscoelastic and elastic inversion. The result from the two inversions is shown in Figure 1, where the original reflector is compared to reflectors predicted by elastic and viscoelastic inversion. It is clear that the result from the elastic inversion is quite poor. The wavenumber spectra of the reflectors yield more insight to the differences. The wavenumber spectra of the three reflectors are shown in Figure 2. We can see an almost perfect match in the range where the reflector is illuminated by the source wavelet for the viscoelastic case but poor reconstruction in the elastic case.

Analysis of Estimation Results.—Both modeling and inversion were done with a constant reference velocity in 1-D. This enables us to easily switch between wavenumber and frequency domain, which makes it possible to compare the wavenumber response of the different estimated reflectors (Figure 2) with propagation effects, due to the viscoelastic medium, derived in the frequency domain. These propagation effects are the likely cause for the incorrect estimate found from the elastic inversion using the viscoelastic seismogram.

For 1-D constant velocity/attenuation medium it is possible to derive a simple expression for the effect on different frequency components in the seismogram. The different components in the frequency spectra decay in time according to

$$e^{-\omega t \frac{\tau \omega \tau_\sigma}{1+\omega^2 \tau_\sigma^2}}, \tag{16}$$

for a viscoelastic medium with a constitutive relation corresponding to a standard linear solid. Since there is only one reflector it is possible to approximate the time t in equation (16) by dividing the distance from the receiver to the reflector by the velocity in the medium.

The above effect should be possible to track in the inverted results if an incorrect value for the attenuation in the media was used, e.g., elastic inversion for viscoelastic (realistic) seismogram, and should in other words cause erroneous estimation of reflectors. Dividing the wavenumber spectra for an elastically estimated reflector with the wavenumber spectra for a viscoelastically estimated reflector should yield a rough approximation to the inverse of the function in equation (16). This is shown in Figure 3. The ratio between the two wave number spectra has only been calculated on the interval where the spectra have a good support. The ratio of the wavenumber spectra is oscillating around the predicted curve which suggests that the erroneous result is due to neglect of the propagation effects (attenuation and dispersion) for the elastic inversion.

Effect of Attenuation and Reflector Depth on Estimation Results

It is naturally more difficult to estimate reflectors with inversion in viscoelastic media than in elastic media, since waves in anelastic media are attenuated and eventually will diffuse into less coherent energy. Simple 1D experiments in constant reference parameter (velocity, density etc.) media should answer some initial questions concerning resolution ability of inversion in attenuating media. What, if anything will be more difficult to estimate in a highly attenuative media compared to a non-attenuative elastic media.

To address these questions we administered an experiment, where we produced synthetic seismograms by modeling in media with different Q. The seismograms were then inverted with the Q used during modeling. The other parameters (bulk modulus, density, reflector, source) were the same as in the previous experiment and the Q:s in the media were $Q = \infty$ (elastic), and $Q \approx 50$ and 100. Since the constant parameter 1D media was used it is possible as before to present the results in the frequency (wavenumber) domain, Figure 4. It is clearly more difficult to estimate higher frequencies in an attenuative medium. There is a perfect match in the frequency range where the source is illuminating the reflector for the elastic case. The inversion process can't match the higher frequencies in the attenuating medium, though. The effect increases with increasing attenuation, which is clear in the close-up in Figure 5. The effect depends on depth as well, since the same experiment performed with a reflector placed at a shallower depth, with the same frequency content, will yield a better match between true and estimated reflectors, Figure 6. For an elastic medium there is no difference between the estimated spectra, Figure 7.

The results suggest that the eigenvalues of high frequency components of reflectors are decreased in a anelastic medium and therefore are more difficult to estimate. The effect seems to be connected to propagation length (or depth of reflectors). The result is not too surprising since constant Q media attenuates high frequencies more than lower and that the effect is more pronounced for longer propagation.

Depth Sensitivity of Layered Media Inversion

One way to further investigate the sensitivity of viscoacoustic inversion to depth is to create a model consisting of several reflectors located at different depths. Use the model to produce a synthetic seismogram and use the seismogram in the inversion algorithm to get an estimate of the reflectors. The estimate would illuminate problems with inversion for reflectors at different depth.

We produced a synthetic seismogram by viscoelastic modeling, Figure 8. The created model consisted of four distinct reflectors which were perturbations in bulk modulus δK, see Figure 9. $\delta\rho = \delta\tau = 0$, $\rho = 2.6\ g/cm^3$, and $\tau = 0.05$ were constant throughout the model. The τ-value corresponds to a minimum Q of approximately 40. K was set so that the velocity in the model was constant $2.0\,km/s$ down to $250\,m$ and then linearly increasing by $(2.7\,m/s)/m$. The source was a Ricker wavelet, with a center frequency of $240\,Hz$, initiated at a depth of $100\,m$. The seismogram was used as input for the inversion. The result from the inversion is shown in Figure 9, where the original reflectors are compared to reflectors predicted by inversion. The deeper reflectors are less well resolved. Figure 10 shows a close-up of the deepest reflector. The predicted reflector is clearly underestimated. The side-lobes in the estimates are due to the finite frequency content of the source wavelet, cf. results above.

Analysis and Improvement of Estimation Results.—The inversion tries to fit the simulated seismogram as well as possible to the measured (or observed) seismogram. Since viscoelastic (realistic) media attenuate propagating waves, later arrivals (corresponding to deeper reflectors) yield smaller amplitudes than earlier arrivals, see Figure 8. Hence later arrivals have less effect on the seismogram as well as on the residual. Deeper reflectors correspond, losely speaking, to smaller eigenvalues of the forward operator. Inversion routines that rely on Krylov-space based iterative methods will favor reflectors corresponding to large eigenvalues i.e., estimate these correctly at an earlier stage in the iterative method. The common solution to this problem is to use a pre-conditioner, i.e. a change of variables in model space. We use instead a change of variables in data space: we pointwise multiply the seismogram by an increasing function of time to counter the attenuation. This is more accurately called post-conditioning. A crude approximation to the viscoelastic attenuation as a function of time is,

$$e^{-t \frac{\tau}{2 \tau_\sigma}}. \tag{17}$$

Hence, the seismogram should be multiplied by the reciprocal of (17) before inversion. The output of the linearized forward map and the input of the adjoint have also to be multiplied by the same gain function. Figure 11 shows true and predicted reflectors, resulting from such inversion. The same number of iterations were performed as for the result shown in Figure 9 . The close-up of the deepest reflector, Figure 12, shows a much better agreement than before (Figure 10).

Multiparameter Inversion (AVO)

The virtue of seismic inversion is to, not only produce an image of the subsurface (as for instance migration), but also yield estimates of physical parameters such as velocity and density. The goal of Amplitude Variation with Offset (AVO) studies is exactly the same. The often offset dependent reflection amplitude is used to deduce relative or exact values for material parameters in AVO studies. Inversion thus implicitly combines two sources of information (methods): imaging (migration) and measurement of physical parameters (AVO).

Rescent studies imply that viscoelastic effects can have a large impact on AVO results, (Martinez, 1993), (Samec and Blangy, 1992). A straight forward method for a more thorough investigation is to study the impact of different amounts of attenuation on inversion results, where correct and incorrect amounts of attenuation are used.

To investigate the impact of attenuation on the results of multiparameter inversion we set up two experiments. In the first experiment linearized synthetic data was produced for four different values of attenuation shown in Table 1. The background density was constant $2.6 g/cm^3$, Q constant, and the background velocity was increasing with depth and implemented through the bulk modulus as shown in Figure 13. The perturbed bulk modulus and density are shown in Figure 14 and 15 respectively. The synthetic data was used as input for the inversion, where the correct values for bulk modulus, density, and attenuation was used. After 20 conjugate residual steps the residual was about or below 3 percent of the original value for all of the four cases of attenuation. Figure 16 shows the estimation results for bulk modulus, reflector 1, where $Q \approx \infty$, 100, 50. The result are in all essential the same for all values of attenuation. The result for $Q \approx 200$ has been omitted, since the result is the same as for other Q-values. The results for higher Q-values might contain higher frequency components as was the case for the 1D experiment. The same is true for the estimated density, reflector 1, in Figure 17. Figure 18 and 19 show the estimated result for the second reflector. Here it is possible to see the effect of no postconditioning. The size of the estimated reflector decreases with increasing attenuation in the medium for the bulk modulus. The size of the reflector increases with increasing attenuation for the density, though, and is negative where the bulk modulus reflector is positive and vice versa. The second density reflector should actually be zero, but the present combination of bulk modulus and density yield an equivalent result for the given geometry and source wavelet. The result clearly indicates smaller eigenvalues for the deeper reflectors and thus they are less well determined. An effect which increases with increasing attenuation. The results again stress the importance of postconditioning and show as well that it is possible retrieve reflectors equally well in elastic and attenuating media, as long as the correct value for the attenuation is known.

In the second experiment we produced synthetic data for $Q \approx 100$. The synthetic data was used to invert for perturbed bulk modulus and density with correct and incorrect amount of attenuation in the reference medium. Q was approximately, ∞, 200, 100, and 50 in the four inversions, see Table 2. The same model for reference bulk modulus and density, and perturbed bulk modulus and density as in the first experiment was used. The residual was less than 4 percent of the original value for all inversion rounds after 20 conjugate residual steps. Figure 20 shows the estimated first bulk modulus reflector. Estimated reflectors are positioned at wrong locations, and amplitudes and shapes are wrong for incorrect values of the reference Q-value. The wavenumber spectra for the reflectors are shown in Figure 24. In the band illuminated by the source wavelet there is a perfect fit for the reflector with correct Q, whereas it is overestimated for a too small Q and underestimated for a too large Q. Figure 21 and 25 show the same behavior for the first density reflector. Figure 22 and 23 just adds to the general conclusion. The corresponding wavenumber spectra in Figure 26 and 27 show that the illuminated passband is smaller for the deeper reflector, due to attenuation and mute. The width of the passband can be increased by performing a larger number of iterations. Figure 27 shows a particularly interesting result. There is actually no density reflector, and this is evident in the passband for reflector estimated with the correct Q, but a reflector is predicted, even in the passband, in the two other cases with Q too high or too low. The result is not only an estimation error (wrong shape/value) but also an interpretation error. A density reflector would be predicted where there was none.

Reflectors are generally consistently overestimated with too low reference Q-values and underestimated with too high reference Q-values. The density seems to be a more robust parameter than the bulk modulus. The reflectors are also incorrectly positioned, since an incorrect Q-value changes the dispersive nature (velocity) of the medium. Unless the correct Q-value is known it is possible to make not only estimation errors, but also interpretation errors. It is clearly necessary to accurately know the correct amount of attenuation in the medium to be able to retrieve accurate parameter values.

Removal of Multiple Reflections through Modeling

A recurring problem in seismic experiments (especially marine exploration) are multiples (multiple reflections). These are created by two large reflectors, where a significant part of the energy of a transmitted elastic wave is reflected. Wave energy will bounce between these reflectors and leave clearly visible energy in a seismogram. The most common multiple reflection in seismic data is created by the water bottom and surface in marine experiment. The water bottom multiple can be viewed as a false reflection that has to be removed from the seismogram before applying techniques such as normal moveout correction, migration, and inversion to find an image of the subsurface through the seismogram. The water bottom multiple do, on the other hand, contain useful information about the relationship between source strength and reflectivity, and removal of the multiple will most likely introduce errors in the remaining data. Explicit multiple removal is thus not an ideal solution.

Inversion techniques are based on explicit forward models for wave propagation and thus it is possible to explicitly model an underlying multiple reflection. Necessary information for correct water bottom multiple modeling is the acoustic velocity and density in the water, and the P-, S-wave velocity and density in the water bottom. These are fortunately fairly well known or easily measured quantities compared to velocities and densities in deep sediments and crust. Multiple modeling is straight forward for non-linear global inversion algorithms (apply algorithm immediately to the data), but is slightly more involved for linearized inversion algorithms. Linearized algorithms model only primary reflections and it is therefore necessary to model the multiple reflection in the background/reference field. Hence, the reference velocity field will not be smooth but contain a discontinuity (water/water bottom). The discontinuity in the reference velocity will create a multiple in the reference field and thus the output from the linearized forward model contains multiple energy. Hence, it is possible to match the energy from the multiples with a linearized model and find a correct reflectivity model through linearized inversion.

To evaluate the method we created synthetic $\tau - p_s$ domain data using the velocity model in Figure 28. It clearly contains a discontinuity which could be thought of as the discontinuity between water and sediments. The data (seismogram) in Figure 29 clearly contains multiple energy at 320 ms and 390 ms. The seismogram has been muted to remove the direct wave, which is indicated in the Figure 29.

The data was inverted with two different background velocity models. One which was continuous (Figure 30) and one which contained the water/sediment discontinuity (Figure 31). The continuous model was created so that the kinematics would be identical to the original model at the two small reflectors at about 200 and 400 m depth.

The goal was to recover the the two small deeper reflectors, which could be assumed to have a linear influence on the data. Since the waterbottom reflection is present in the seismogram, the inversion result will contain an estimate of the waterbottom as well. This estimate will naturally be quite different from the original waterbottom step, since the step-discontinuity waterbottom reflector contains an infinite frequency range and the source does not support such a range.

Figure 32 show the results of inversion with the two different reference velocity models. In both of the inversions the final residual was about or less than 1 percent of the original residual (20 conjugate residual steps). A range of 30 slowness values were used in the modeling, which corresponds to large offsets in the original non-transformed data, Figure 29. There is no obvious trace of the multiple reflection in any of the final estimates. The reflector estimated using the smooth velocity model seems less well determined than the one estimated with the discontinuous velocity model, Figure 33. The inversion should naturally lead to the same estimate of the reflectors, since the kinematic velocity is correct. The presence of multiples resulted in a different estimate, even though they do not show up as false reflectors. The multiples have been suppressed by stacking. When a large range of slowness values are used it is possible to just stack out the multiple energy as long as the kinematic background velocity is correct. The raw stacking procedure might yield an incorrect estimate, though.

The inversion estimates change if the range of slowness values is decreased to the 10 first, Figure 34. In both of the inversions the final residual was about or less than 0.2 percent of the original residual (50 conjugate residual steps). The multiple energy does show up as false reflectors in the estimate obtained using the smooth velocity model. The estimates of the true reflectors are also almost identical, as they should be, for the two different velocity models, Figure 35. The multiple energy is clearly present in the smooth velocity estimate, though, Figure 36. Two false reflectors are present which perfectly correspond to the multiples in the data.

Multiple removal through raw stacking power is not a good option for inversion. The result of the inversion will most likely be erroneous, even though no multiples will be visible in the final estimate. If the multiples are modeled through the reference fields no such problems will arise. Multiple energy can be removed from data which has no or small stacking power (i.e., too few receivers and too small offsets were used), through modeling. A kinematically correct but smooth reference velocity model will yield false reflectors, in inversion estimates, corresponding to multiples in the data.

CONCLUSIONS

We have described a viscoelastic linearized inversion algorithm for layered media. Through a suite of numerical experiments we found that the error in estimates of reflectors can be severe and AVO results will not be reliable if anelastic effects are neglected. High frequency content of reflectors will be difficult to estimate correctly in highly attenuative media. It seems necessary to post-condition seismograms to correctly estimate deep reflectors. Multiples cannot be removed correctly through raw stacking power. Multiple removal through modeling seems to be an interesting option, especially for data with no or small stacking power.

ACKNOWLEDGMENTS

This research was supported by ONR grant N00014-89-J1115, the Schlumberger Foundation, and The Rice Inversion Project. TRIP Sponsors for 1994 are Advance Geophysical, Amoco Production Co., Conoco Inc., Cray Research Inc., Discovery Bay Co., Exxon Production Research Co., Interactive Network Technologies, Mobil Research and Development Corp., and Texaco Inc.

REFERENCES

Blanch, J. O., Robertsson, J. O. A., and Symes, W. W., Viscoelastic finite difference modeling:, Technical Report TR 93-04, Department of Computational and Applied Mathematics, Rice University, 1993.

——— 1993b, Viscoelastic finite difference modeling *in* Kleinman, R., Angell, T., Colton, D., Santosa, F., and Stakgold, I., Eds., Mathematical and numerical aspects of wave propagation:: SIAM, 69–81.

Blanch, J. O., Robertsson, J. O. A., and Symes, W. W., 1995, Modeling of a constant Q: Methodology and algorithm for an efficient and optimally inexpensive viscoelastic technique: Geophysics, page In press.

Bourbie, T., Coussy, O., and Zinzner, B., 1987, Acoustics of porous media: Gulf Publishing Company.

Keys, R. G., and Foster, D. J., 1995, A data set for evaluating and comparing seismic inversion methods: 64th Ann. Internat. Mtg. of Soc. Expl. Geophys., Proceedings of the SEG 1994 postconvention workshop: Comparison of Seismic Inversion Methods to a Single Real Data Set, to appear.

Lion, J. L., 1971, Optimal control of systems governed by partial differential equations: Springer-Verlag.

Martinez, R. D., and McMechan, G. A., 1991, τ-p seismic data for viscoelastic media - Part 2: Linearized inversion: Geophys. Prosp., **39**, 157–181.

Martinez, R. D., 1993, Wave propagation effects on amplitude variation with offset measurements: A modeling study: Geophysics, **58**, 534–543.

Robertsson, J. O. A., Blanch, J. O., Levander, A. R., Webb, H. F., and Goff, J. A. 2-d and 3-d viscoelastic seafloor reverberation modeling:. Abstract for the 1993 ARSRP meeting at Scripps Institute, La Joll, CA, 1993.

Robertsson, J. O. A., Blanch, J. O., and Symes, W. W., 1994, Viscoelastic finite-difference modeling: Geophysics, **59**, 1444–1456.

Samec, P., and Blangy, J. P., 1992, Viscoelastic attenuation, anisotropy and AVO: Geophysics, **57**, 441–450.

Shuey, R. T., 1985, A simplification of zoeppritz equations: Geophysics, **50**, 609–614.

Tarantola, A., 1988, Theoretical background for the inversion if seismic waveforms, including elasticity and attenuation *in* Aki, A., and Wu, R. S., Eds., Scattering and attenuation of seismic waves, PAGEOPH.:: Birkhäuser Verlag, Basel.

TABLES

Attenuation	Modeling τ	Inversion τ
$Q \approx 50$	0.04	0.04
$Q \approx 100$	0.02	0.02
$Q \approx 200$	0.01	0.01
$Q = \infty$	0.00	0.00

TABLE 1. Amount of attenuation used in modeling and inversion in experiment 1.

Attenuation	Modeling τ	Inversion τ
$Q \approx 50$	0.02	0.04
$Q \approx 100$	0.02	0.02
$Q \approx 200$	0.02	0.01
$Q = \infty$	0.02	0.00

TABLE 2. Amount of attenuation used in modeling and inversion in experiment 2.

FIGURES

FIG. 1. The true reflector with two inversion estimates. Solid - True reflector, Dashed - Viscoelastic estimate, Dotted - Elastic estimate.

FIG. 2. Frequency content of the true reflector and the two estimates. Solid - True reflector, Dashed - Viscoelastic estimate, Dotted - Elastic estimate.

FIG. 3. Ratio of the wavenumber spectra of two estimates and the predicted effect from attenuation in medium, equation (16). Solid - Ratio of the wavenumber spectra of two estimates, Dashed - The reciprocal of the predicted effect for decay.

FIG. 4. Frequency spectra of true and estimated reflectors. Solid - True Reflector. Dashed - Estimated reflector for $Q = \infty$ medium. Dotted - Estimated reflector for $Q \approx 50$ medium. Dash-dotted - Estimated reflector for $Q \approx 25$ medium.

FIG. 5. Close-up of frequency spectra of true and estimated reflectors. Solid - True Reflector. Dashed - Estimated reflector for $Q = \infty$ medium. Dotted - Estimated reflector for $Q \approx 50$ medium. Dash-dotted - Estimated reflector for $Q \approx 25$ medium.

FIG. 6. Close-up of frequency spectra of true and estimated reflectors. Solid - True Reflector. Dashed - Estimated reflector for $Q = \infty$ medium. Dotted - Estimated reflector for $Q \approx 50$ medium. Dash-dotted - Estimated reflector for $Q \approx 25$ medium.

FIG. 7. Close-up of frequency spectra of true and estimated reflectors. Solid - True Reflector. Dashed - Estimated reflector for $Q = \infty$ medium. Dotted - Estimated reflector for $Q \approx 50$ medium. Dash-dotted - Estimated reflector for $Q \approx 25$ medium.

FIG. 8. τ-p_s seismogram used in the inversion routine. Note that the seismogram

contains surface multiples.

FIG. 9. True and estimated reflectors without post conditioning. Solid - True reflectors, Dashed - Estimated reflectors.

FIG. 10. True and estimated reflector without post conditioning. Solid - True reflector, Dashed - Estimated reflector.

FIG. 11. True and estimated reflectors with post conditioning. Solid - True reflectors, Dashed - Estimated reflectors.

FIG. 12. True and estimated reflector with post conditioning. Solid - True reflector, Dashed - Estimated reflector.

FIG. 13. The reference bulk modulus. It is constant to about 250 m depth and increases then quadratively with depth, which corresponds to a linear increase in velocity.

FIG. 14. The perturbed input bulk modulus. It contains two reflectors.

FIG. 15. The perturbed input density. It contains one reflector at the same depth as the perturbed bulkmodulus' first reflector.

FIG. 16. The estimated bulk modulus for different reference Q. Reflector 1. Solid - True reflector, Dashed - $Q = \infty$, Dotted - $Q \approx 100$, Dash-dotted - $Q \approx 50$.

FIG. 17. The estimated density for different reference Q. Reflector 1. Solid - True reflector, Dashed - $Q = \infty$, Dotted - $Q \approx 100$, Dash-dotted - $Q \approx 50$.

FIG. 18. The estimated bulk modulus for different reference Q. Reflector 2. Solid - True reflector, Dashed - $Q = \infty$, Dotted - $Q \approx 100$, Dash-dotted - $Q \approx 50$.

FIG. 19. The estimated density for different reference Q. Reflector 2. Solid - True reflector, Dashed - $Q = \infty$, Dotted - $Q \approx 100$, Dash-dotted - $Q \approx 50$.

FIG. 20. The estimated bulk modulus for different reference Q for data produced with $Q \approx 100$. Reflector 1. Solid - True reflector, Dashed - $Q \approx 100$, Dotted - $Q = \infty$, Dash-dotted - $Q \approx 50$.

FIG. 21. The estimated density for different reference Q for data produced with $Q \approx 100$. Reflector 1. Solid - True reflector, Dashed - $Q \approx 100$, Dotted - $Q = \infty$, Dash-dotted - $Q \approx 50$.

FIG. 22. The estimated bulk modulus for different reference Q for data produced with $Q \approx 100$. Reflector 2. Solid - True reflector, Dashed - $Q \approx 100$, Dotted - $Q = \infty$, Dash-dotted - $Q \approx 50$.

FIG. 23. The estimated density for different reference Q for data produced with $Q \approx 100$. Reflector 2. Solid - True reflector, Dashed - $Q \approx 100$, Dotted - $Q = \infty$, Dash-dotted - $Q \approx 50$.

FIG. 24. Wavenumber spectrum of the estimated bulk modulus for different reference Q for data produced with $Q \approx 100$. Reflector 1. Solid - True reflector, Dashed - $Q \approx 100$, Dotted - $Q = \infty$, Dash-dotted - $Q \approx 50$.

FIG. 25. Wavenumber spectrum of the estimated density for different reference Q for

data produced with $Q \approx 100$. Reflector 1. Solid - True reflector, Dashed - $Q \approx 100$, Dotted - $Q = \infty$, Dash-dotted - $Q \approx 50$.

FIG. 26. Wavenumber spectrum of the estimated bulk modulus for different reference Q for data produced with $Q \approx 100$. Reflector 2. Solid - True reflector, Dashed - $Q \approx 100$, Dotted - $Q = \infty$, Dash-dotted - $Q \approx 50$.

FIG. 27. Wavenumber spectrum of the estimated density for different reference Q for data produced with $Q \approx 100$. Reflector 2. Solid - True reflector, Dashed - $Q \approx 100$, Dotted - $Q = \infty$, Dash-dotted - $Q \approx 50$.

FIG. 28. Velocity model used to create synthetic data (non-linearized modeling).

FIG. 29. Muted $\tau - p_s$ data from modeling. The direct wave is removed through muting. The data contains a clear water bottom multiple at 320 ms and a second multiple at 400 ms. The second multiple is created by a reflection from water bottom - water surface - first reflector.

FIG. 30. The continuous background velocity used for the inversion.

FIG. 31. The discontinuous background velocity used for the inversion.

FIG. 32. True estimated bulk modulus for smooth and discontinuous velocity model. A range of 30 slowness values was used. No immediate indication can be found of the multiple. The solid line shows bulk modulus reflectivity representing the bumps in the velocity model in Figure 28, i.e., the true reflectivity and assumed linear part of the forward model. The dashed line is the estimated result, when the discontinuous background model (Figure 31) was used. The dotted line is the estimated result,

when the smooth background model (Figure 30) was used.

FIG. 33. True estimated bulk modulus for smooth and discontinuous velocity model. A range of 30 slowness values was used. A close-up of the deepest reflector. The reflector estimated with the smooth velocity model seems to be a slightly worse estimated of the true reflector than the estimate obtained with the discontinuous velocity model. The solid line shows bulk modulus reflectivity representing the bumps in the velocity model in Figure 28, i.e., the true reflectivity and assumed linear part of the forward model. The dashed line is the estimated result, when the discontinuous background model (Figure 31) was used. The dotted line is the estimated result, when the smooth background model (Figure 30) was used.

FIG. 34. True estimated bulk modulus for smooth and discontinuous velocity model. A range of 10 slowness values was used. The estimate obtained using the smooth velocity model show two false reflectors between the two true reflectors. The false reflectors are clearly caused by the multiple energy. The solid line shows bulk modulus reflectivity representing the bumps in the velocity model in Figure 28, i.e., the true reflectivity and assumed linear part of the forward model. The dashed line is the estimated result, when the discontinuous background model (Figure 31) was used. The dotted line is the estimated result, when the smooth background model (Figure 30) was used.

FIG. 35. True estimated bulk modulus for smooth and discontinuous velocity model. A range of 10 slowness values was used. A close-up of the deepest reflector. The estimates of the deepest reflector are essentially identical for both velocity models. The solid line shows bulk modulus reflectivity representing the bumps in the velocity model in Figure 28, i.e., the true reflectivity and assumed linear part of the forward model. The dashed line is the estimated result, when the discontinuous background

model (Figure 31) was used. The dotted line is the estimated result, when the smooth background model (Figure 30) was used.

FIG. 36. True estimated bulk modulus for smooth and discontinuous velocity model. A range of 10 slowness values was used. A close-up of the deepest reflector. The estimates of the deepest reflector are essentially identical for both velocity models. The solid line shows bulk modulus reflectivity representing the bumps in the velocity model in Figure 28, i.e., the true reflectivity and assumed linear part of the forward model. The dashed line is the estimated result, when the discontinuous background model (Figure 31) was used. The dotted line is the estimated result, when the smooth background model (Figure 30) was used.

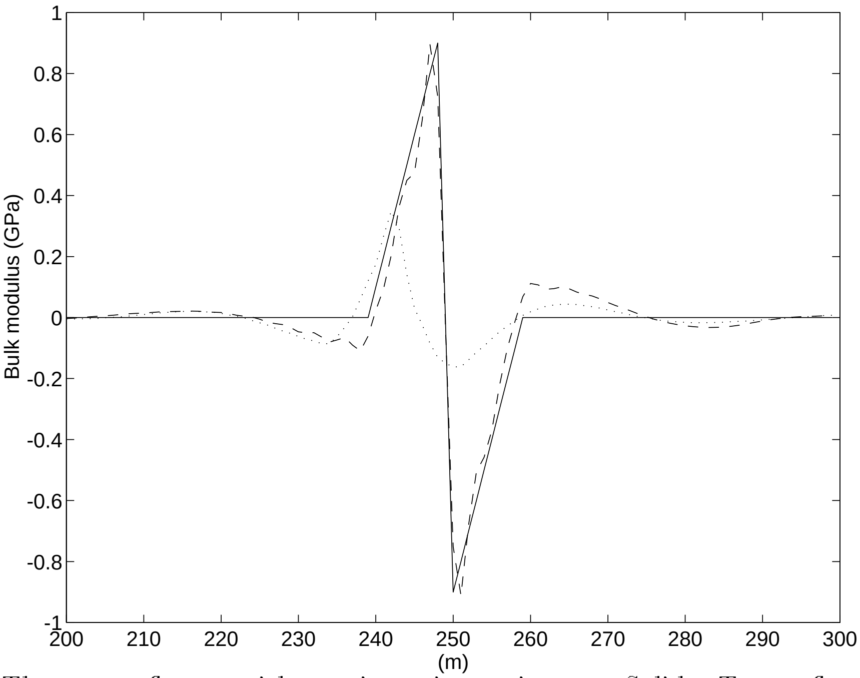

FIG. 1. The true reflector with two inversion estimates. Solid - True reflector, Dashed - Viscoelastic estimate, Dotted - Elastic estimate.

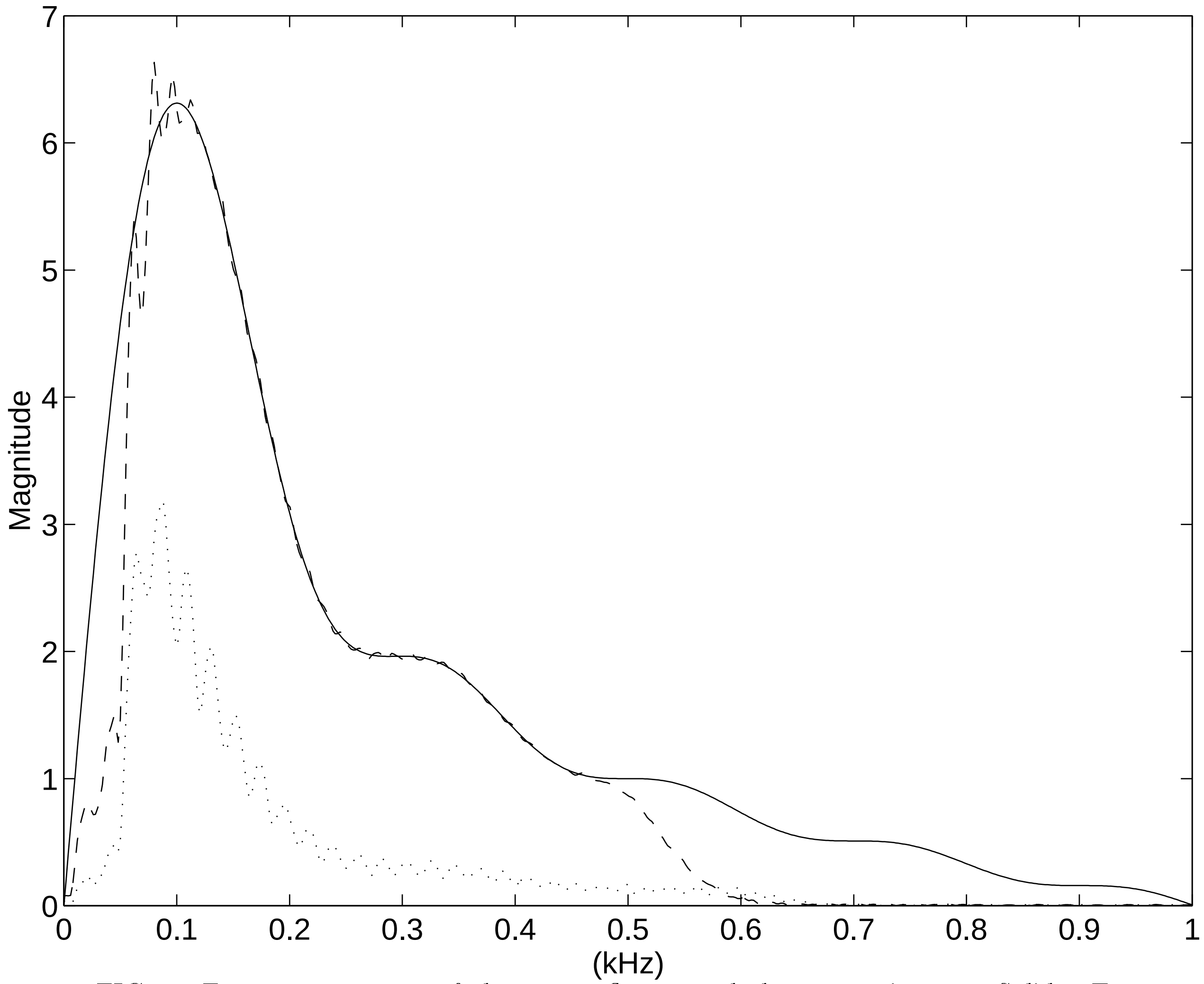

FIG. 2. Frequency content of the true reflector and the two estimates. Solid - True reflector, Dashed - Viscoelastic estimate, Dotted - Elastic estimate.

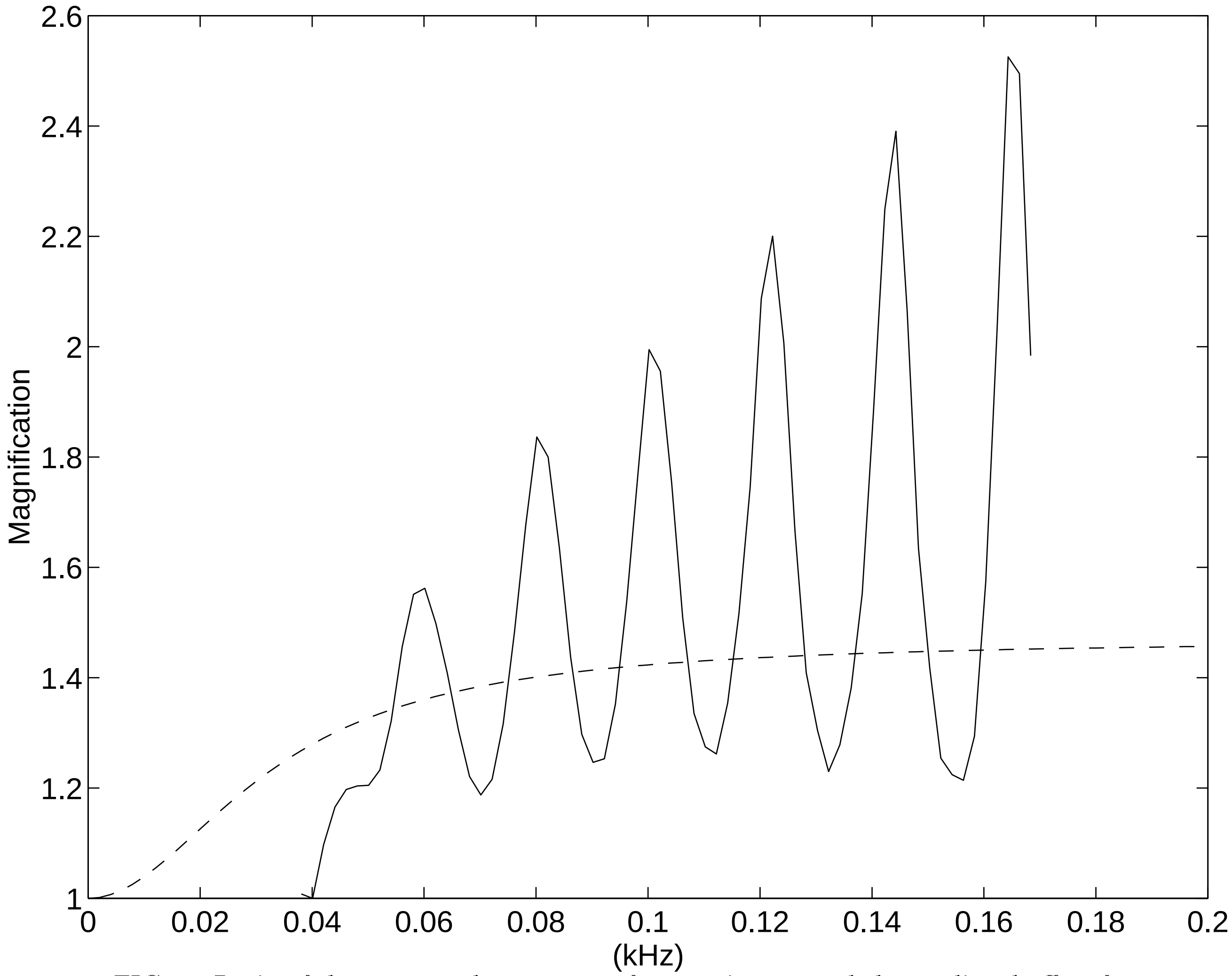

FIG. 3. Ratio of the wavenumber spectra of two estimates and the predicted effect from attenuation in medium, equation (16). Solid - Ratio of the wavenumber spectra of two estimates, Dashed - The reciprocal of the predicted effect for decay.

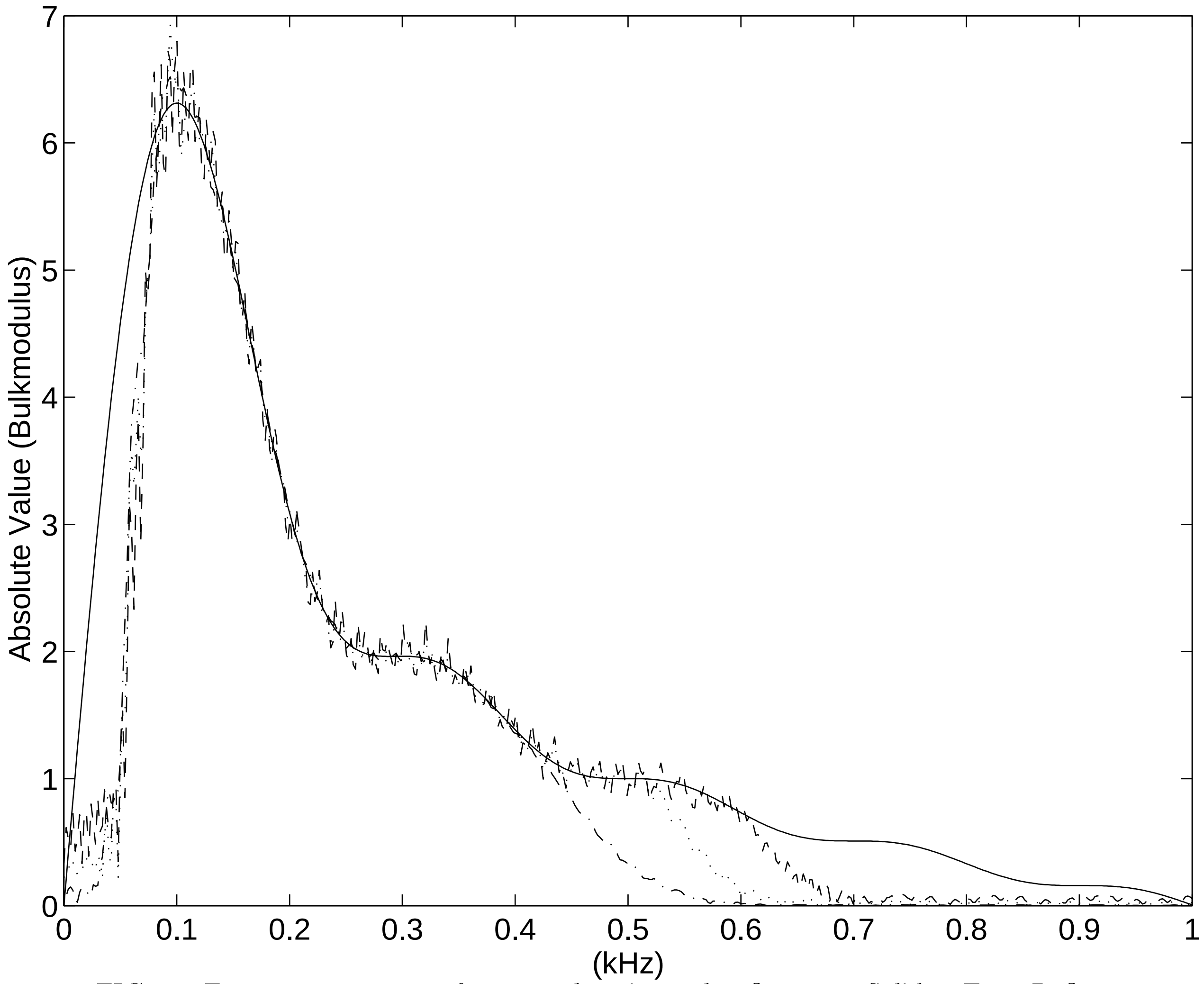

FIG. 4. Frequency spectra of true and estimated reflectors. Solid - True Reflector. Dashed - Estimated reflector for $Q = \infty$ medium. Dotted - Estimated reflector for $Q \approx 50$ medium. Dash-dotted - Estimated reflector for $Q \approx 25$ medium.

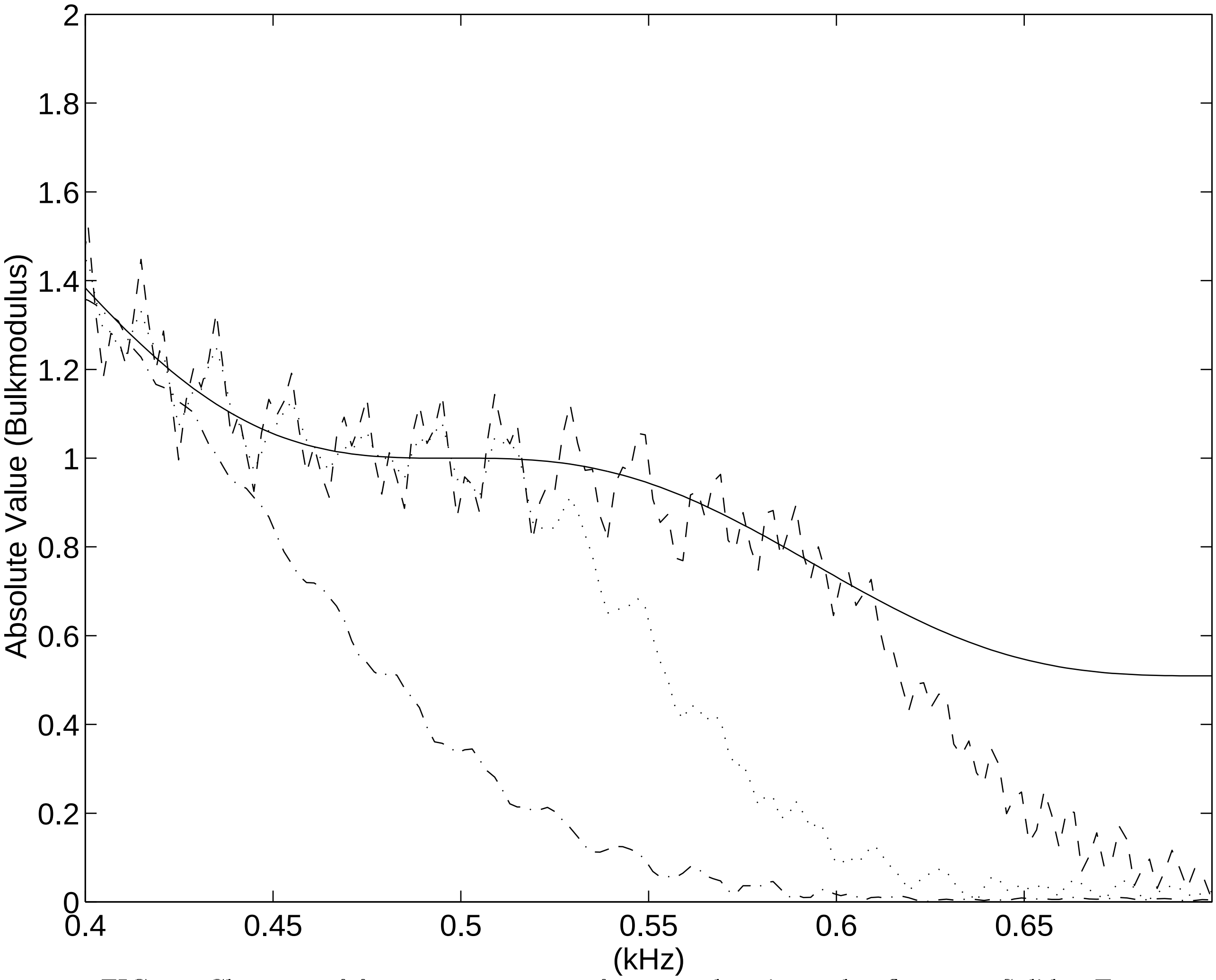

FIG. 5. Close-up of frequency spectra of true and estimated reflectors. Solid - True Reflector. Dashed - Estimated reflector for $Q = \infty$ medium. Dotted - Estimated reflector for $Q \approx 50$ medium. Dash-dotted - Estimated reflector for $Q \approx 25$ medium.

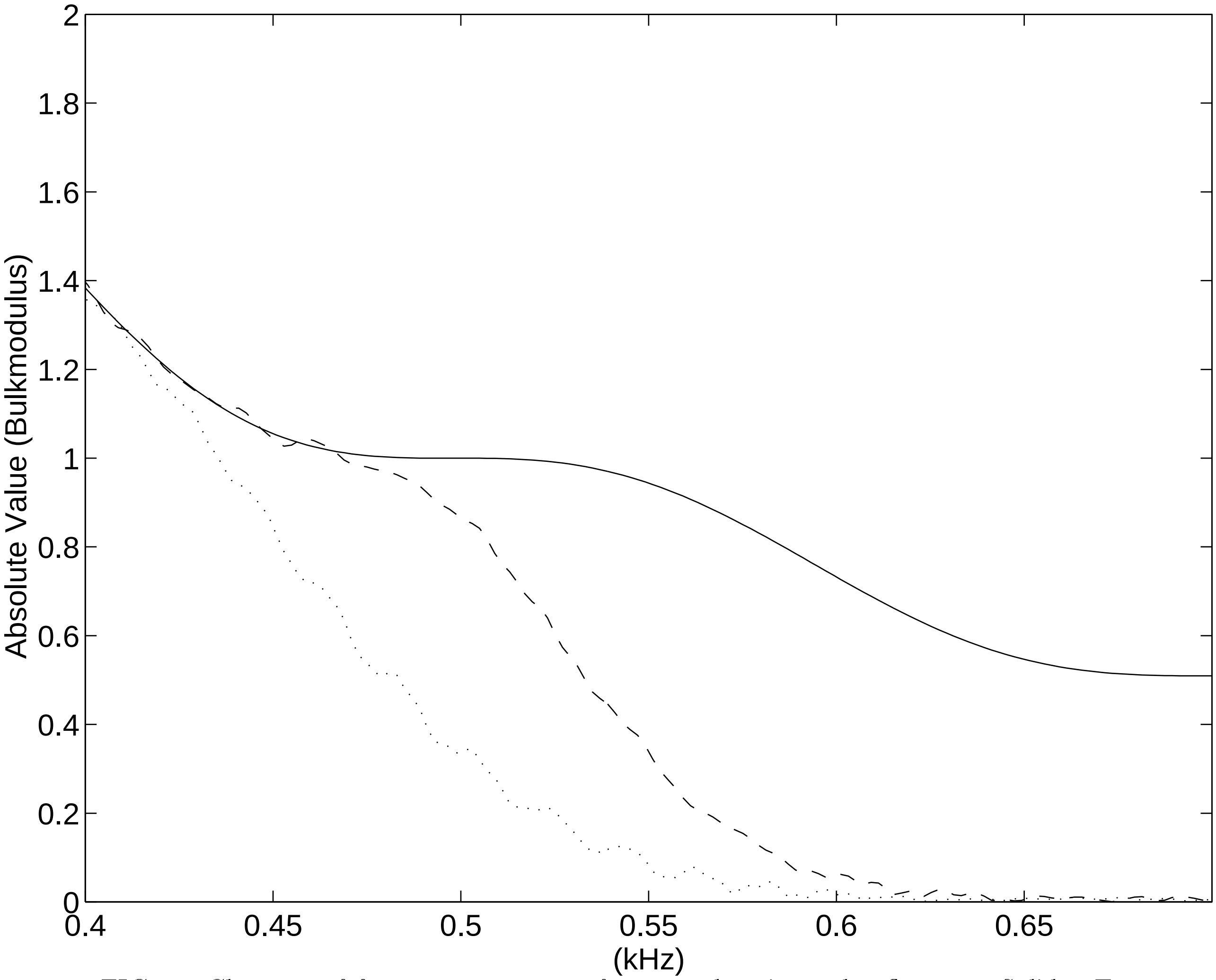

FIG. 6. Close-up of frequency spectra of true and estimated reflectors. Solid - True Reflector. Dashed - Estimated reflector for $Q = \infty$ medium. Dotted - Estimated reflector for $Q \approx 50$ medium. Dash-dotted - Estimated reflector for $Q \approx 25$ medium.

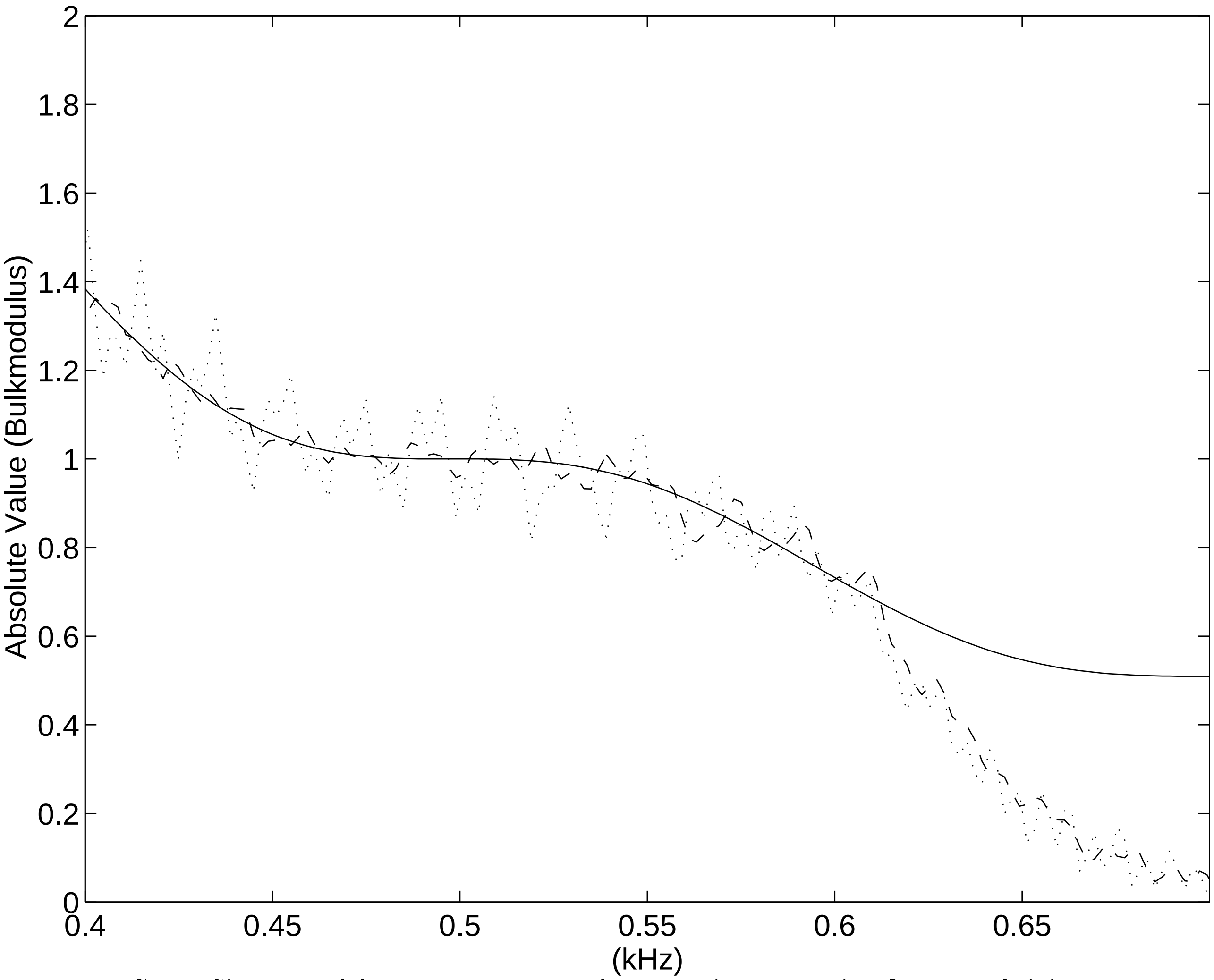

FIG. 7. Close-up of frequency spectra of true and estimated reflectors. Solid - True Reflector. Dashed - Estimated reflector for $Q = \infty$ medium. Dotted - Estimated reflector for $Q \approx 50$ medium. Dash-dotted - Estimated reflector for $Q \approx 25$ medium.

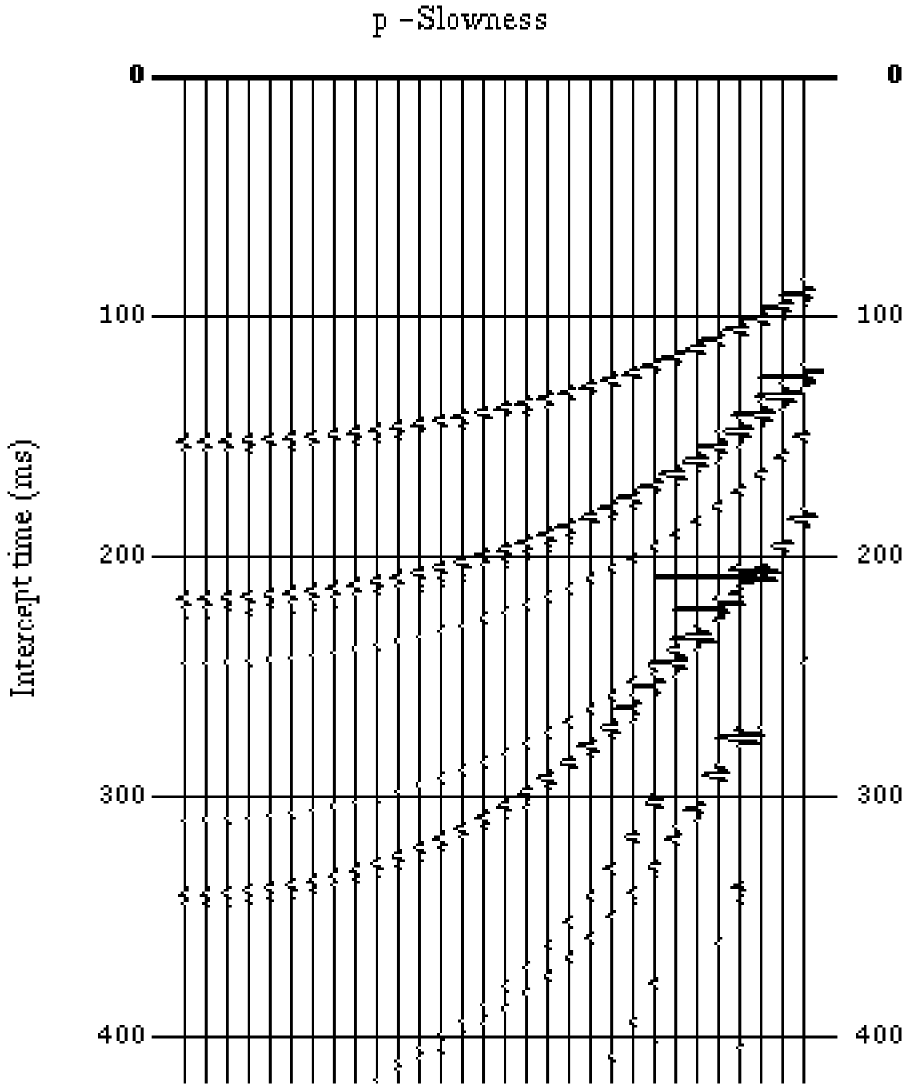

FIG. 8. τ-p_s seismogram used in the inversion routine. Note that the seismogram contains surface multiples.

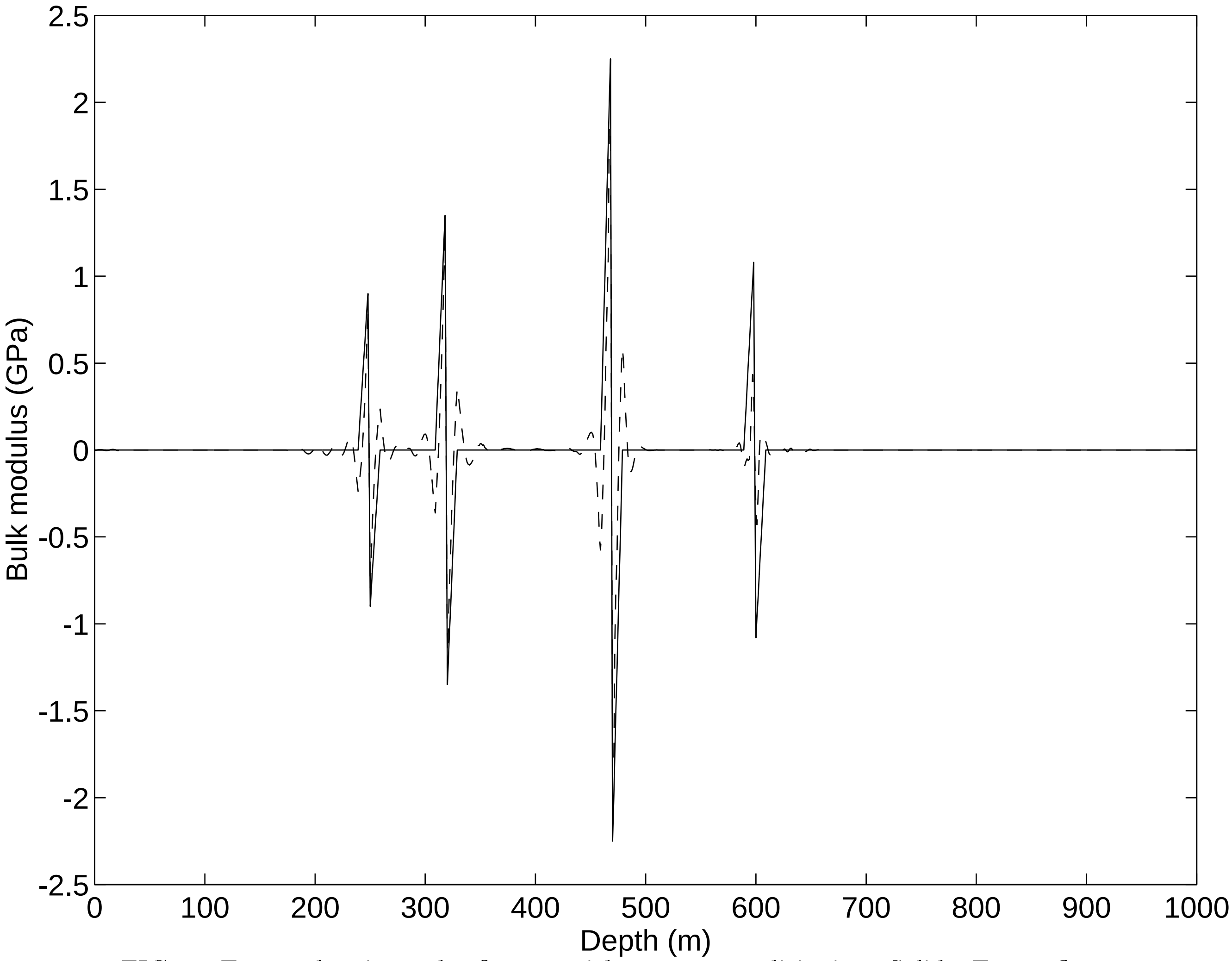

FIG. 9. True and estimated reflectors without post conditioning. Solid - True reflectors, Dashed - Estimated reflectors.

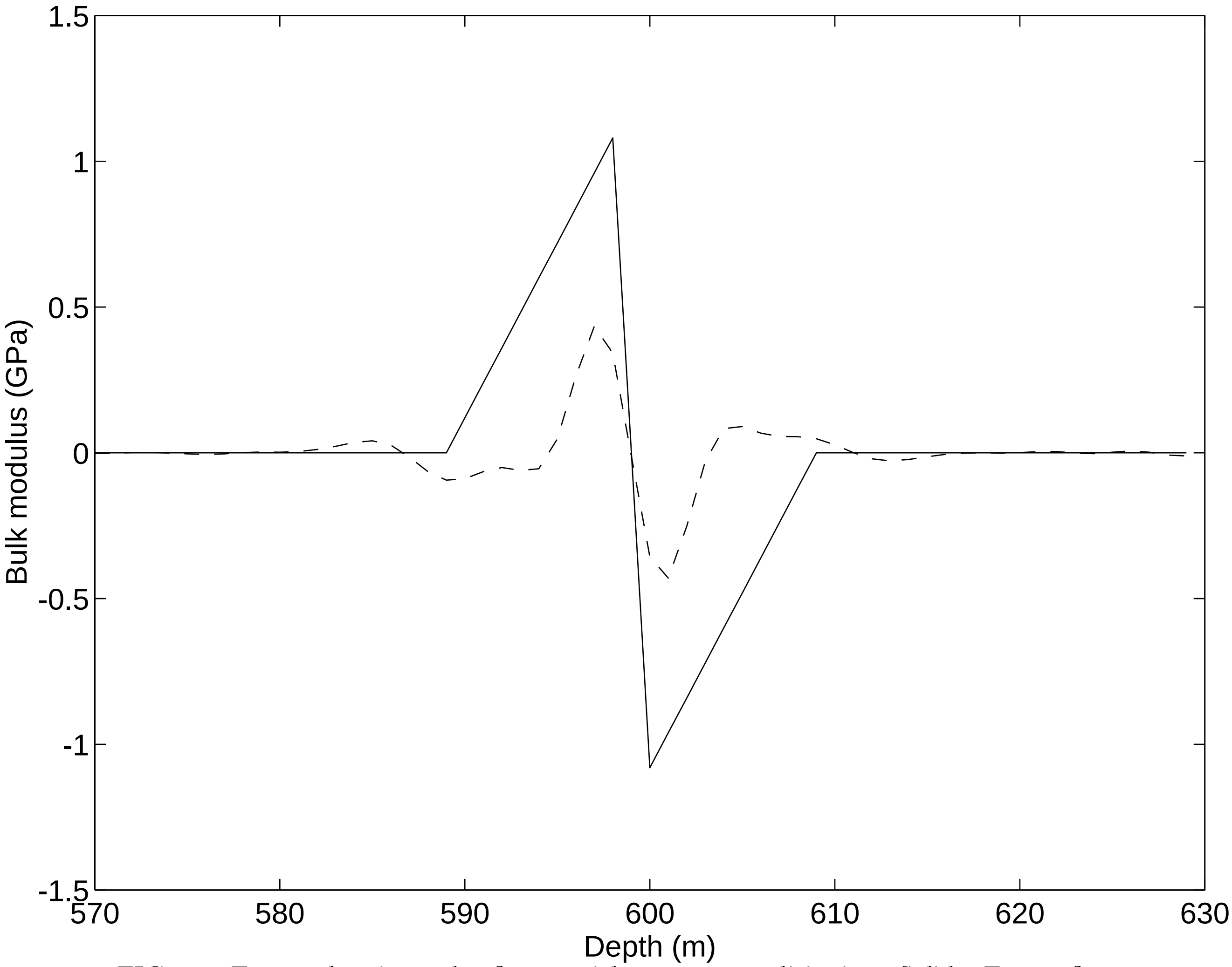

FIG. 10. True and estimated reflector without post conditioning. Solid - True reflector, Dashed - Estimated reflector.

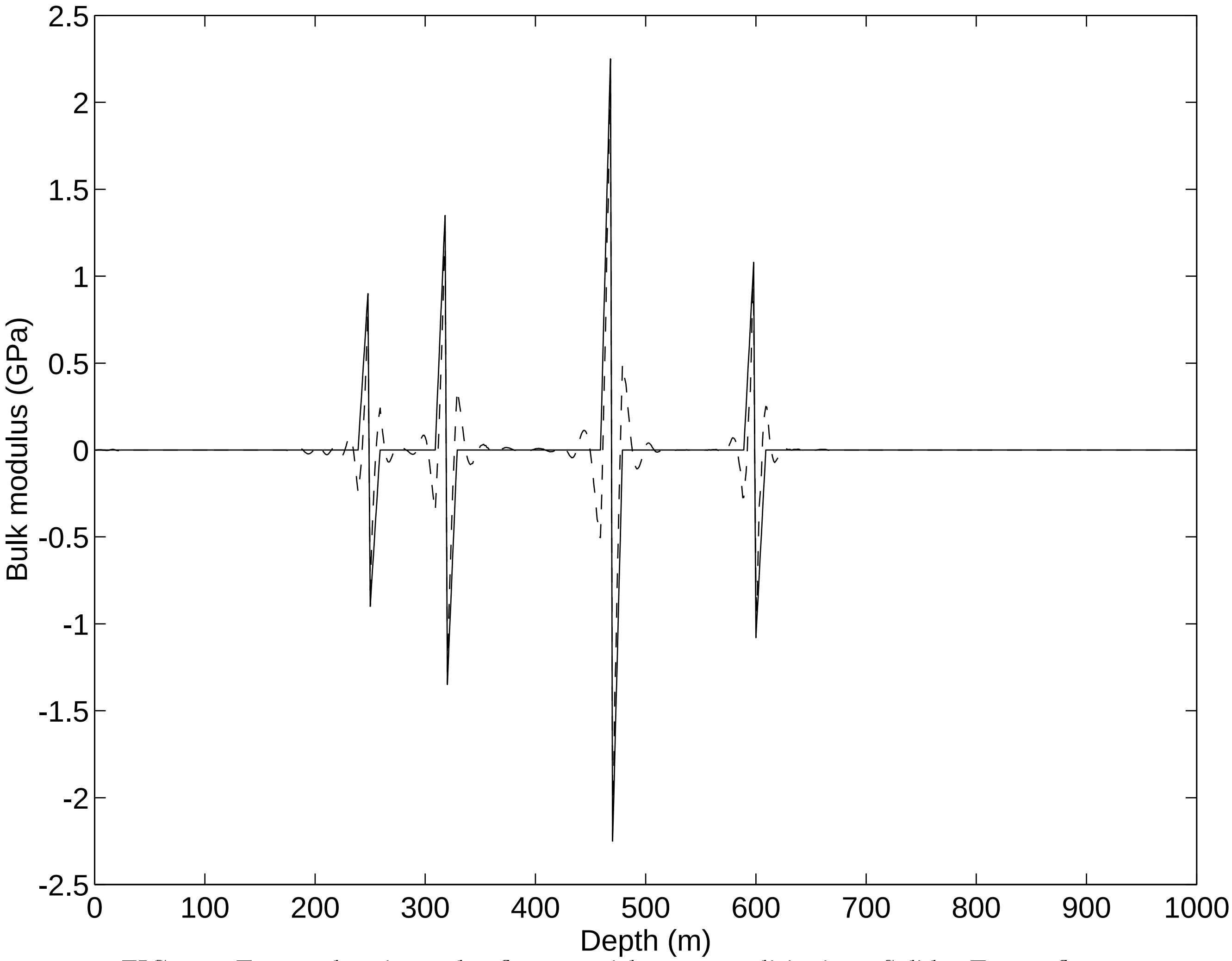

FIG. 11. True and estimated reflectors with post conditioning. Solid - True reflectors, Dashed - Estimated reflectors.

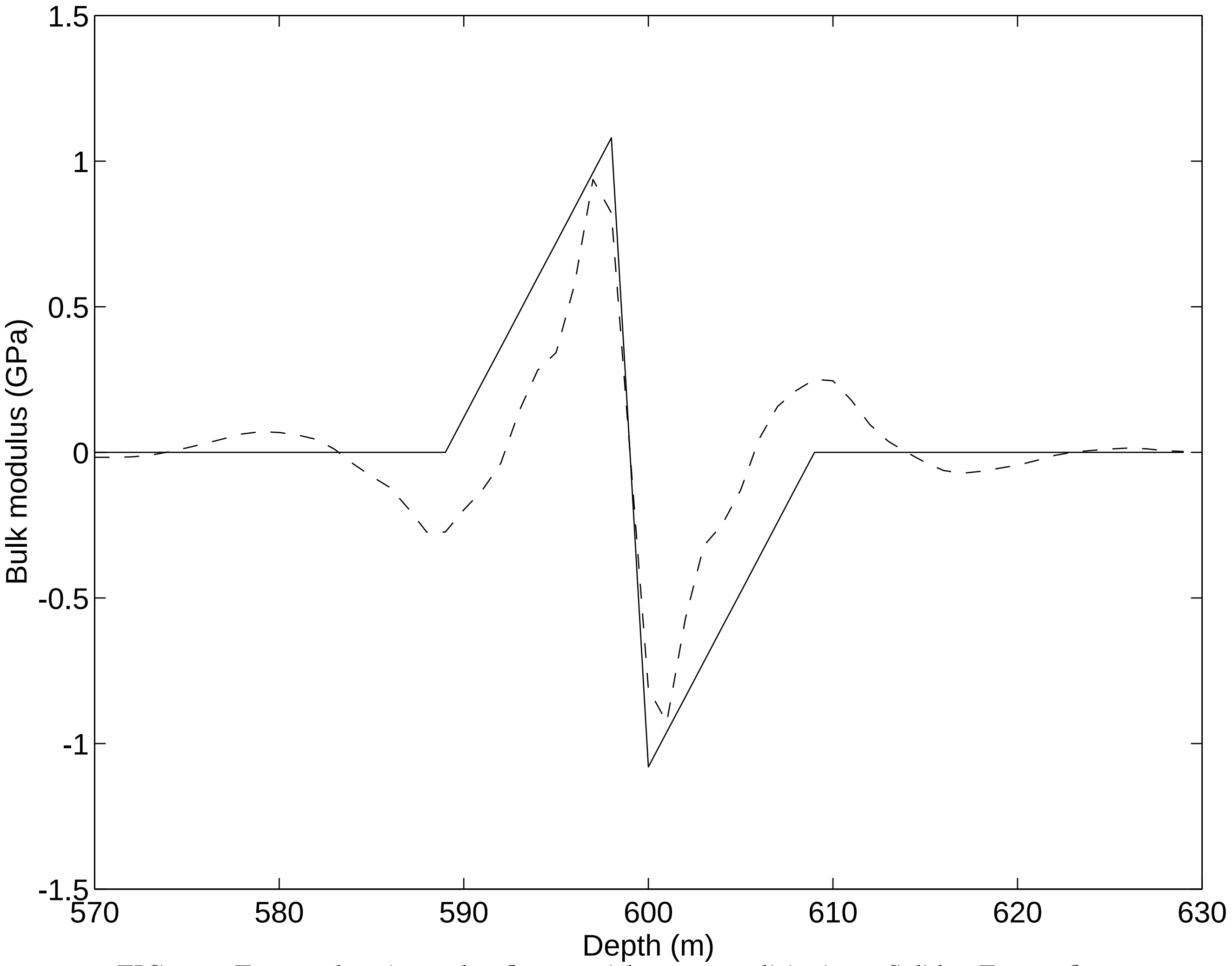

FIG. 12. True and estimated reflector with post conditioning. Solid - True reflector, Dashed - Estimated reflector.

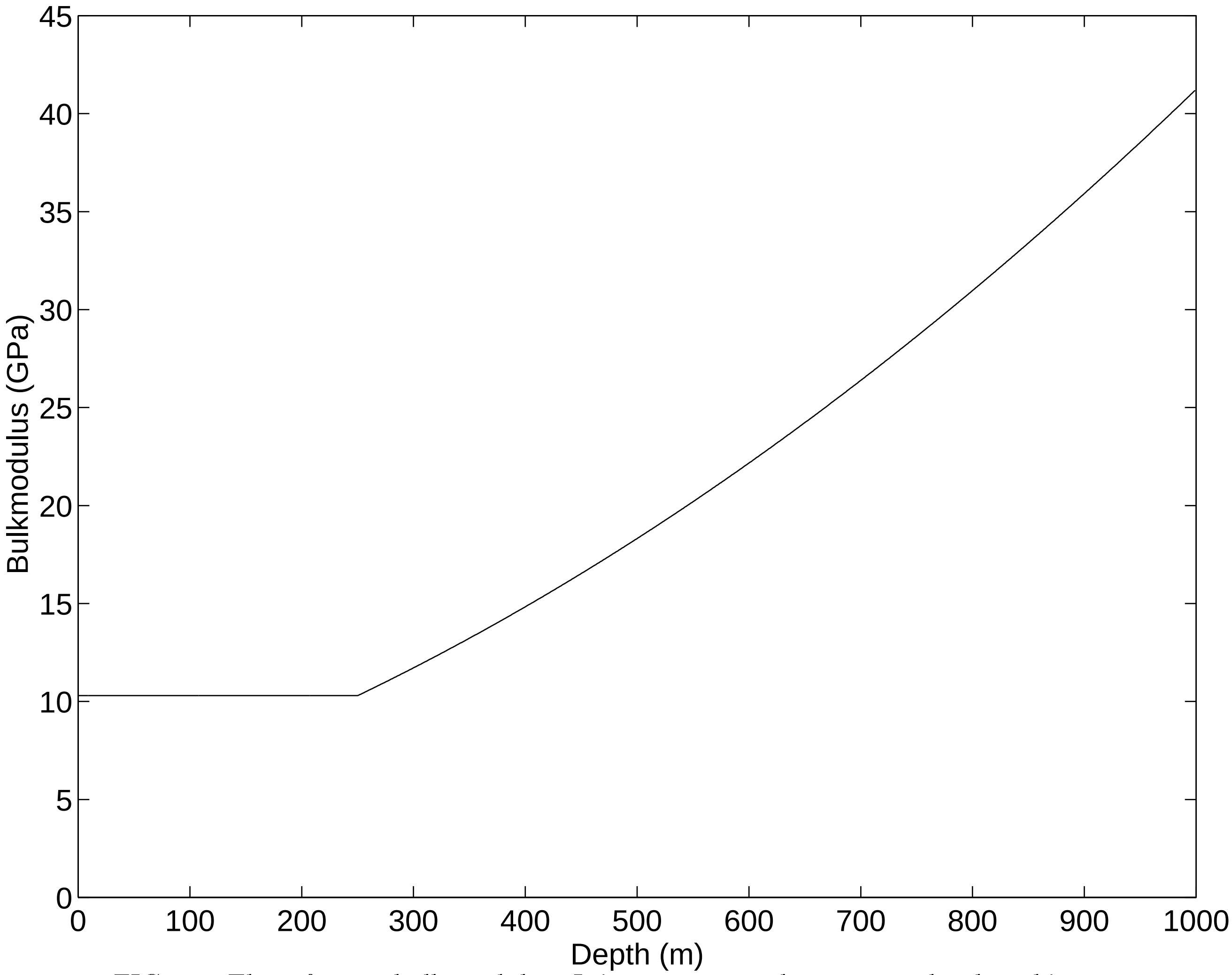

FIG. 13. The reference bulk modulus. It is constant to about 250 m depth and increases then quadratively with depth, which corresponds to a linear increase in velocity.

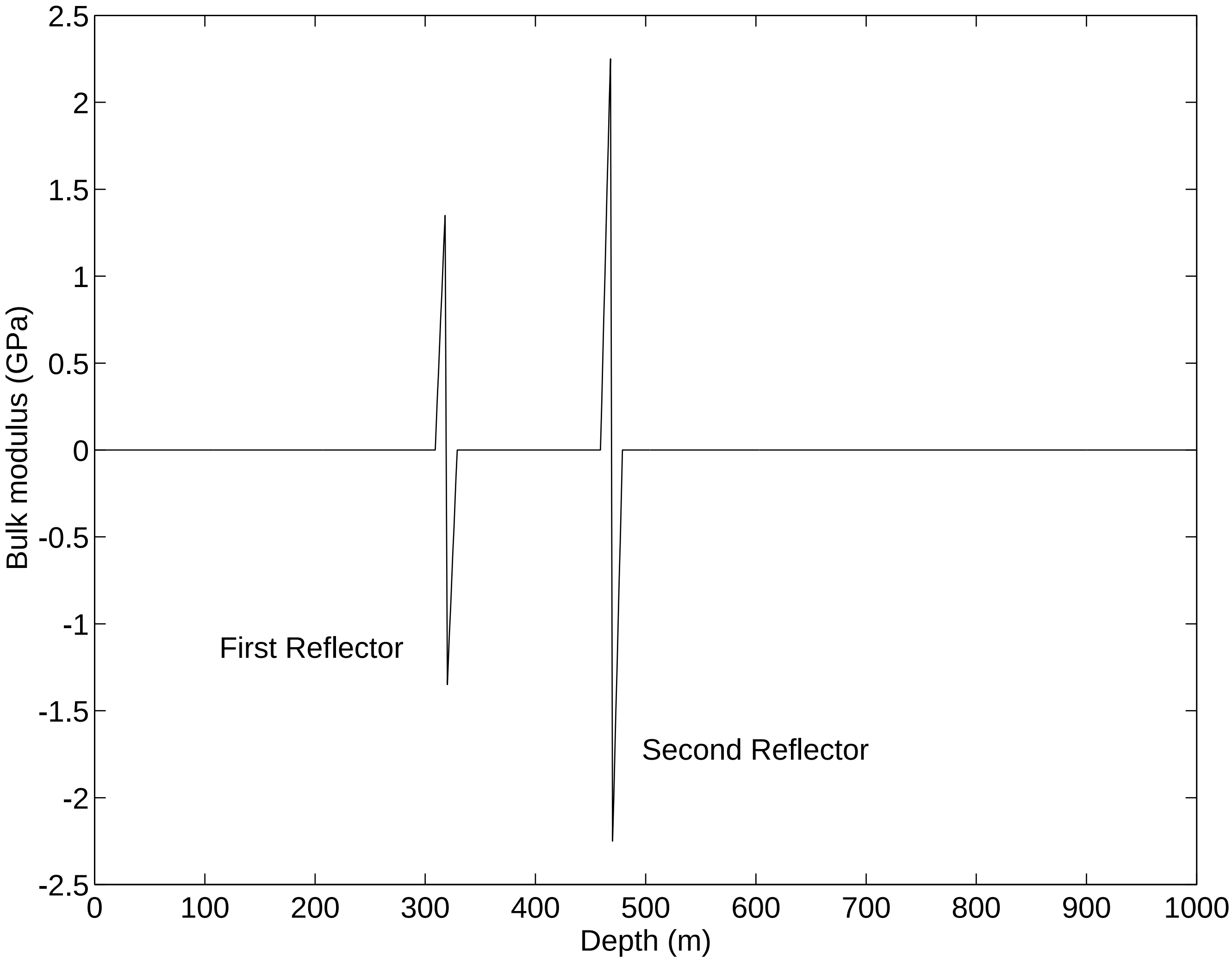

FIG. 14. The perturbed input bulk modulus. It contains two reflectors.

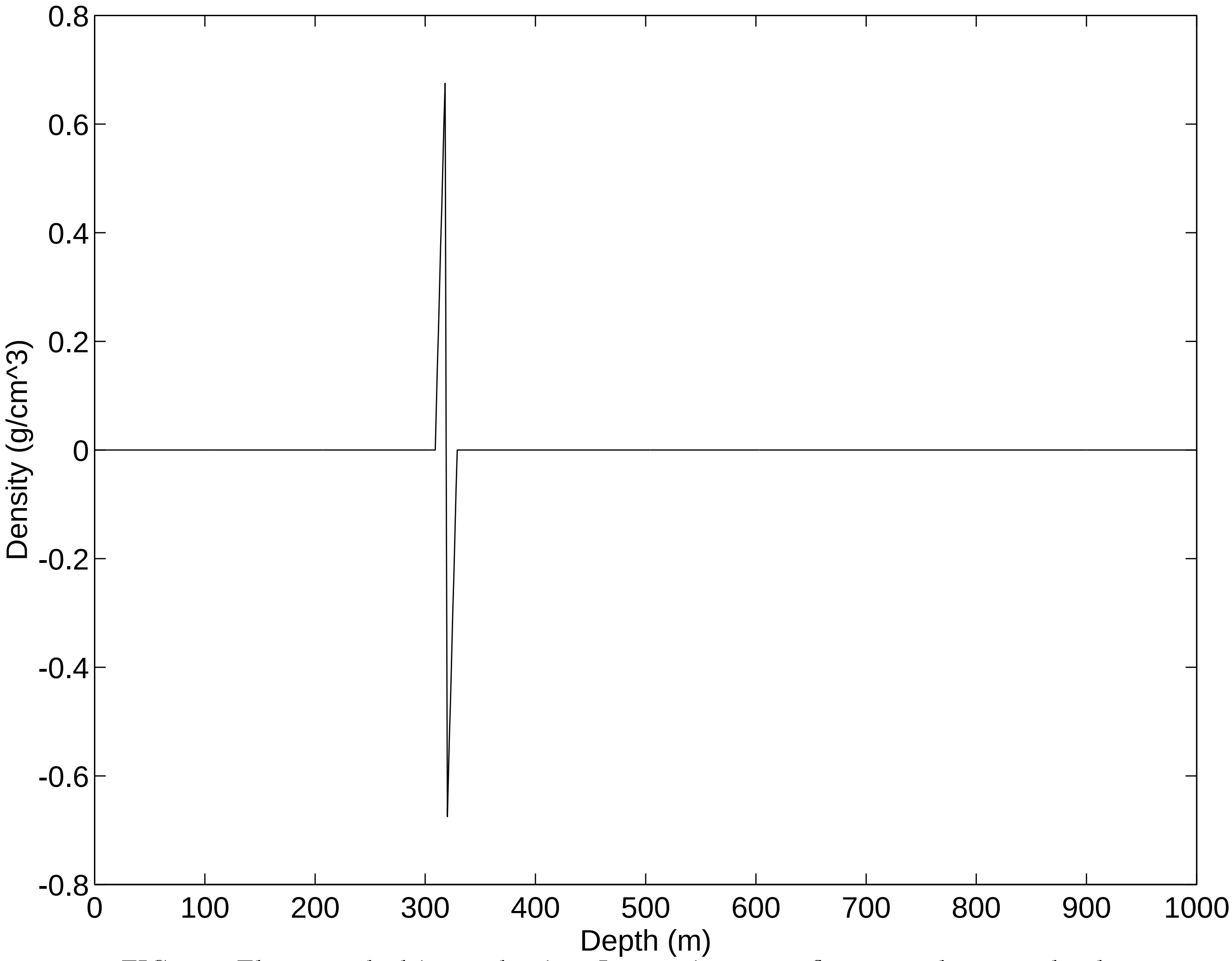

FIG. 15. The perturbed input density. It contains one reflector at the same depth as the perturbed bulkmodulus' first reflector.

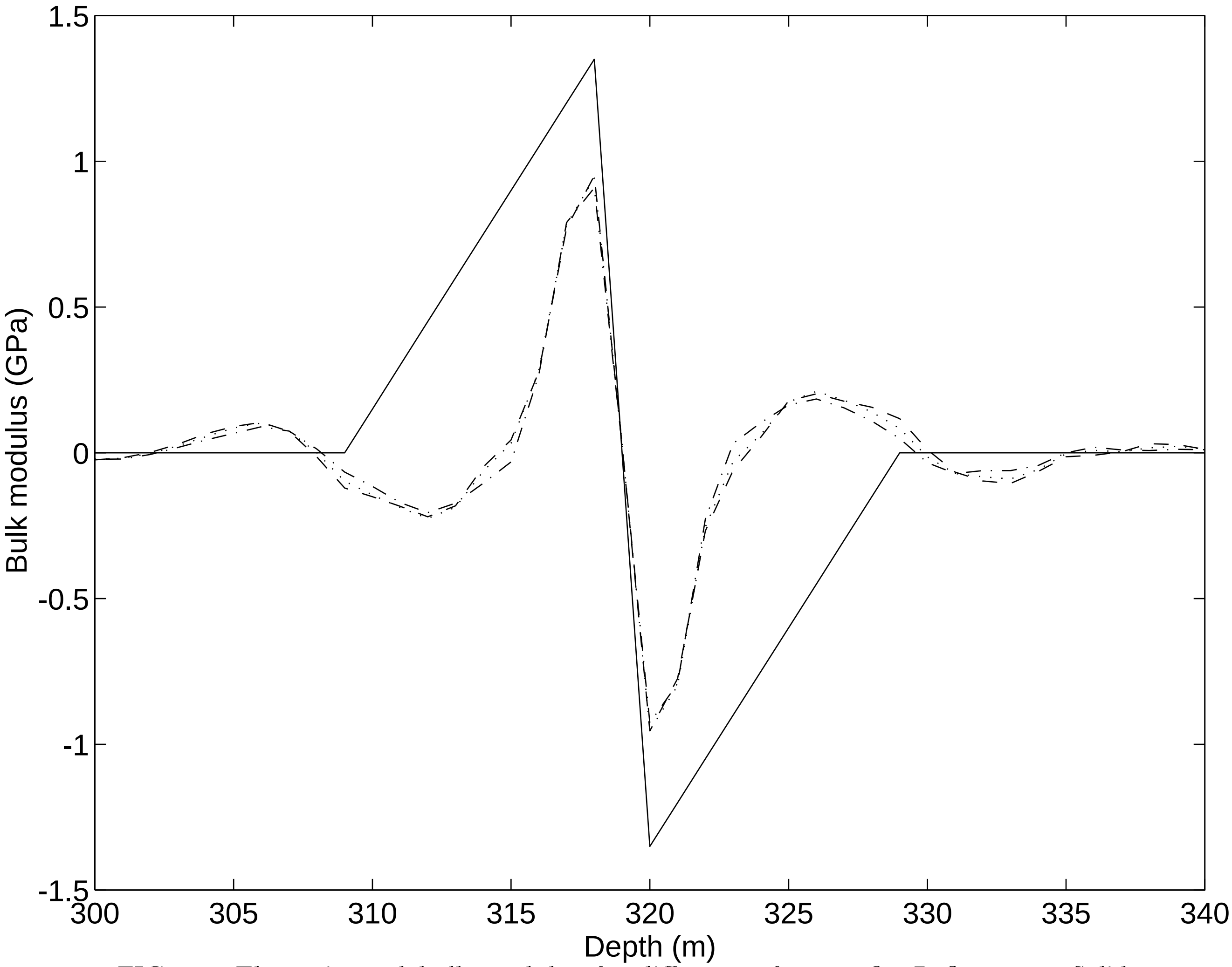

FIG. 16. The estimated bulk modulus for different reference Q. Reflector 1. Solid - True reflector, Dashed - $Q = \infty$, Dotted - $Q \approx 100$, Dash-dotted - $Q \approx 50$.

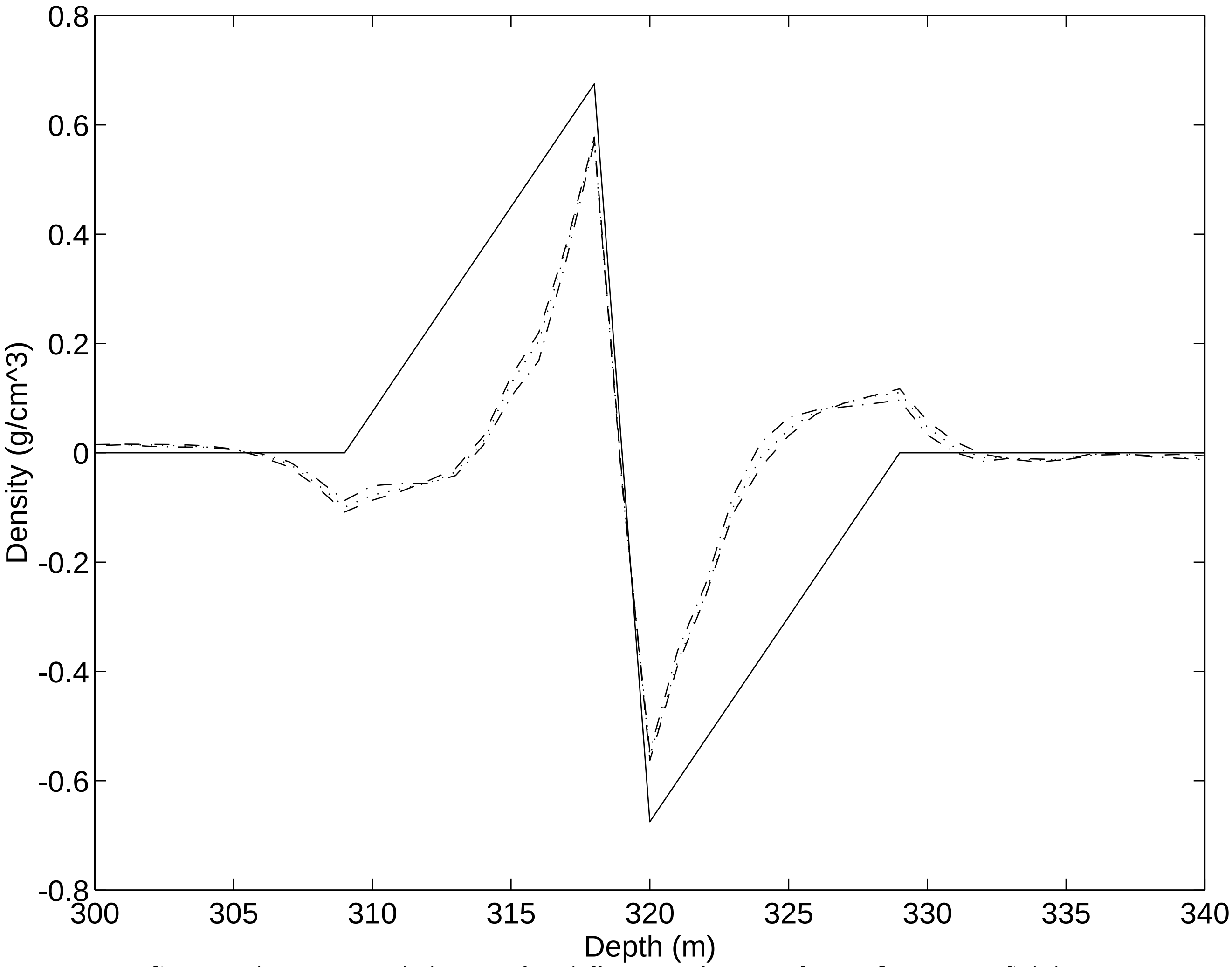

FIG. 17. The estimated density for different reference Q. Reflector 1. Solid - True reflector, Dashed - $Q = \infty$, Dotted - $Q \approx 100$, Dash-dotted - $Q \approx 50$.

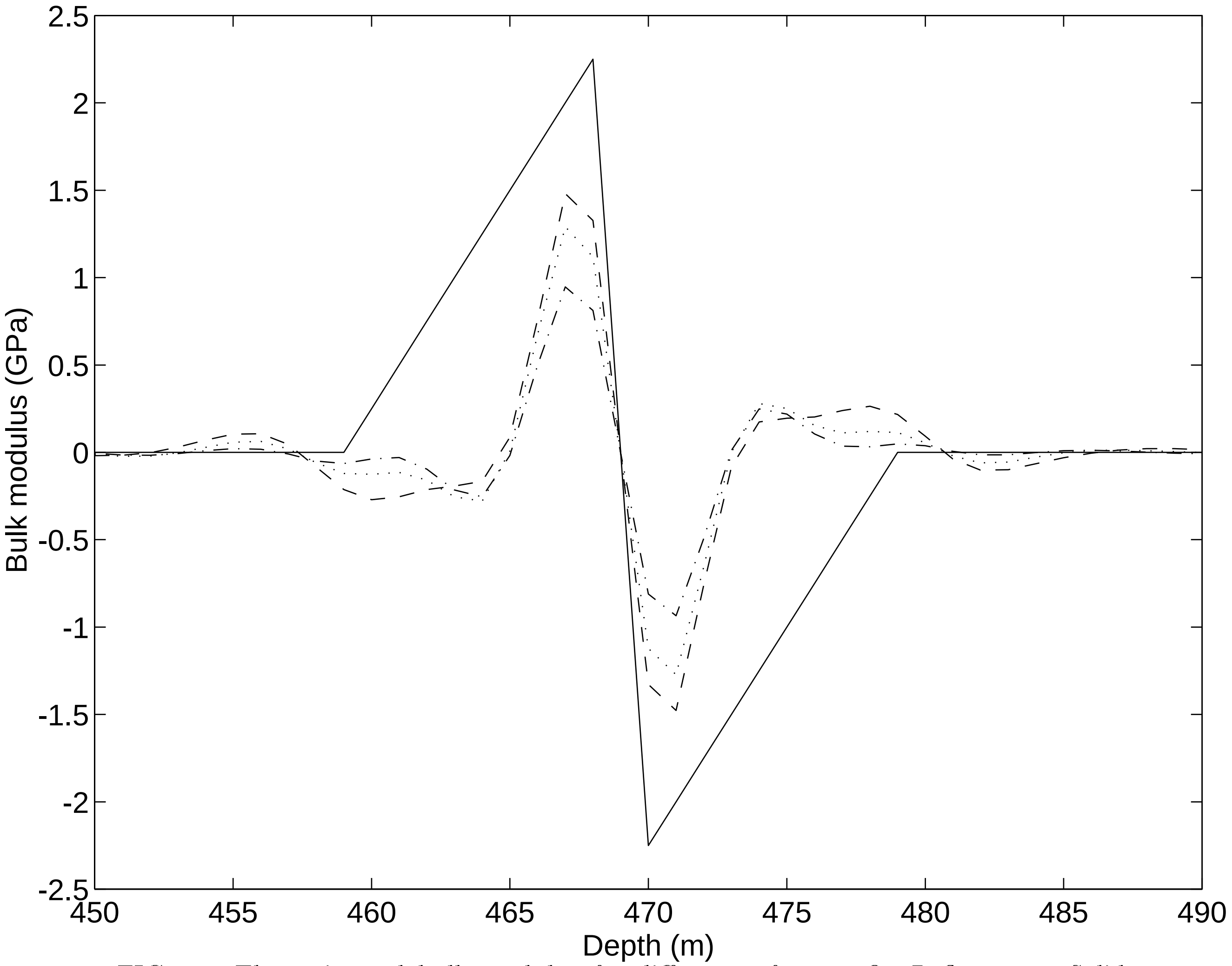

FIG. 18. The estimated bulk modulus for different reference Q. Reflector 2. Solid - True reflector, Dashed - $Q = \infty$, Dotted - $Q \approx 100$, Dash-dotted - $Q \approx 50$.

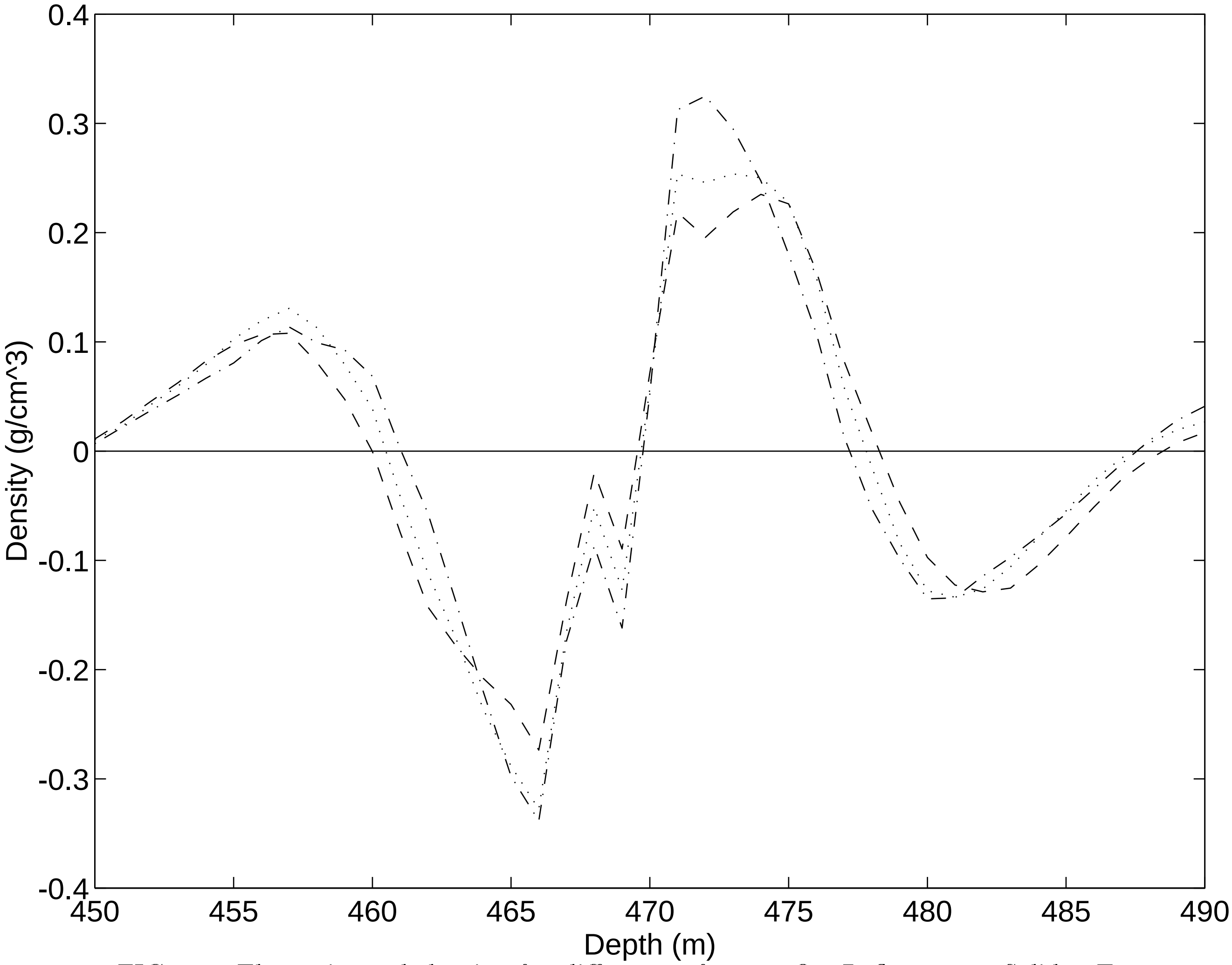

FIG. 19. The estimated density for different reference Q. Reflector 2. Solid - True reflector, Dashed - $Q = \infty$, Dotted - $Q \approx 100$, Dash-dotted - $Q \approx 50$.

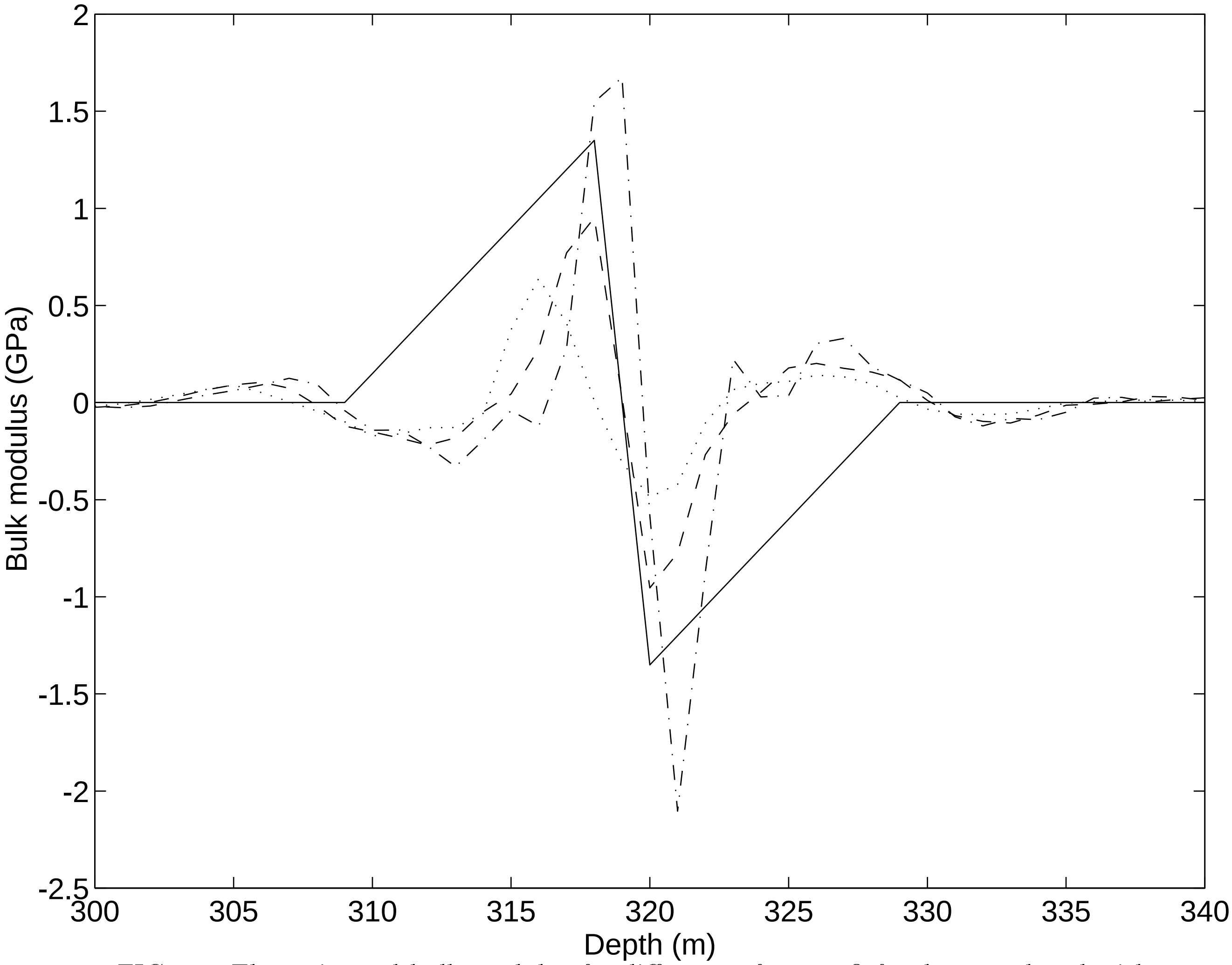

FIG. 20. The estimated bulk modulus for different reference Q for data produced with $Q \approx 100$. Reflector 1. Solid - True reflector, Dashed - $Q \approx 100$, Dotted - $Q = \infty$, Dash-dotted - $Q \approx 50$.

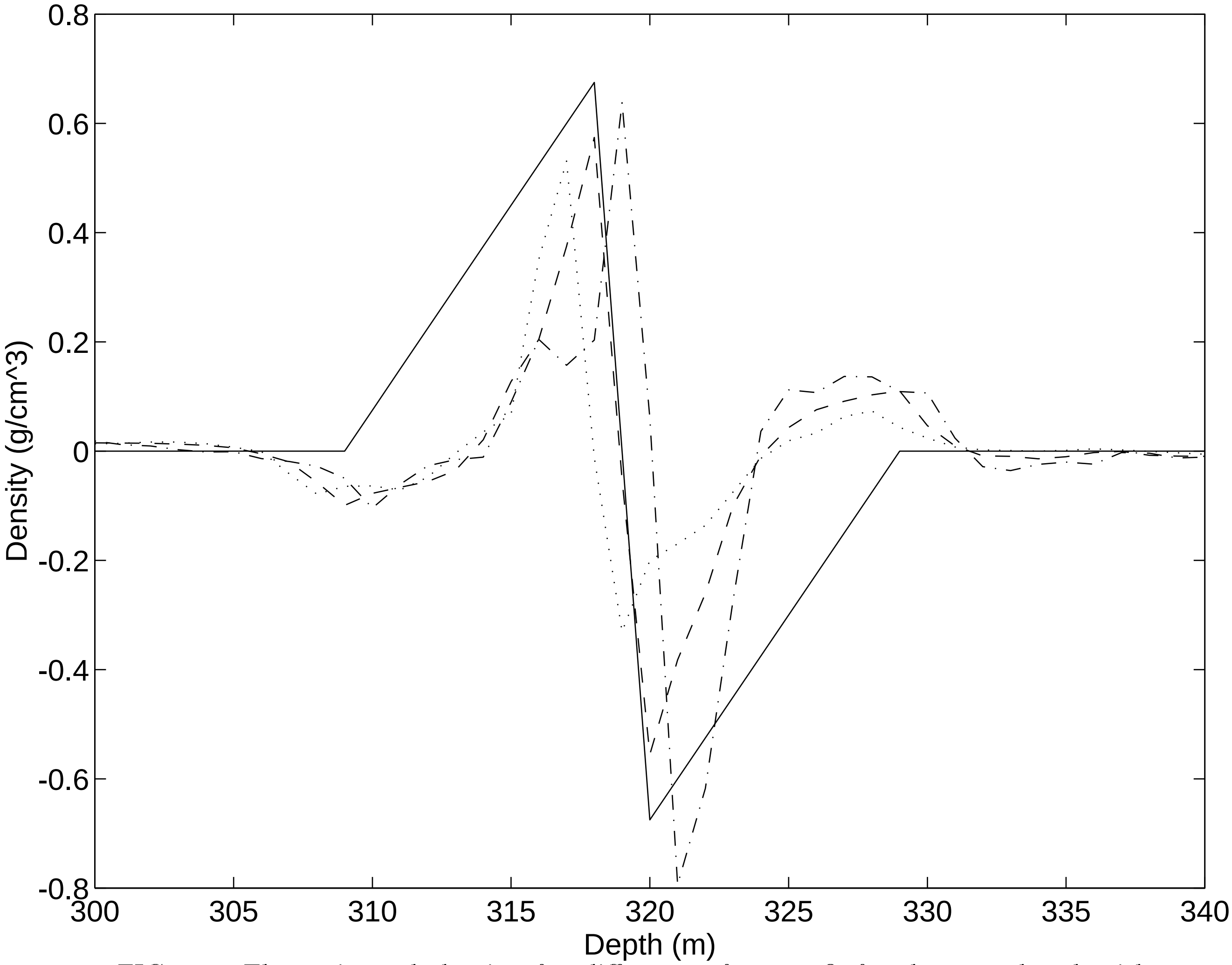

FIG. 21. The estimated density for different reference Q for data produced with $Q \approx 100$. Reflector 1. Solid - True reflector, Dashed - $Q \approx 100$, Dotted - $Q = \infty$, Dash-dotted - $Q \approx 50$.

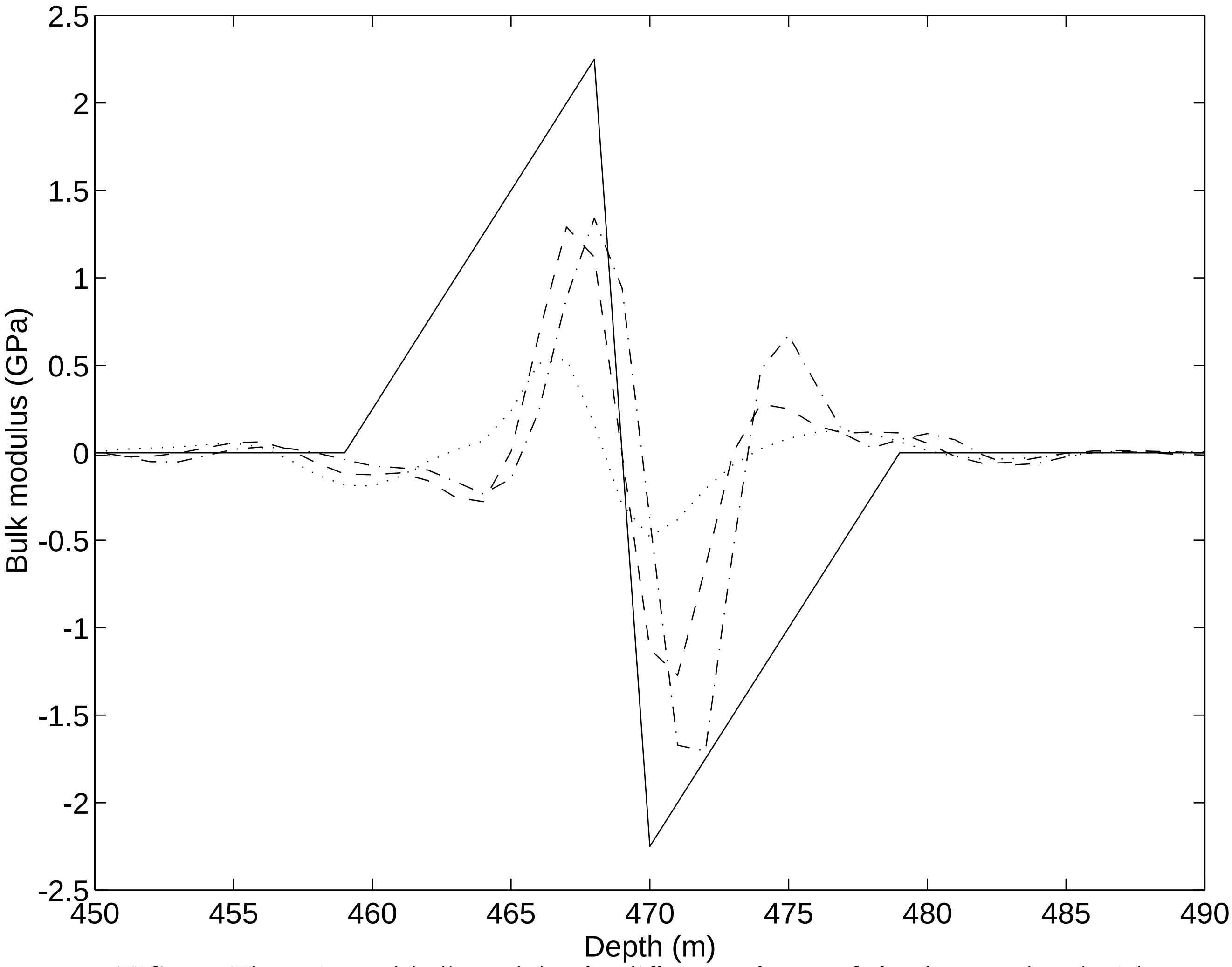

FIG. 22. The estimated bulk modulus for different reference Q for data produced with $Q \approx 100$. Reflector 2. Solid - True reflector, Dashed - $Q \approx 100$, Dotted - $Q = \infty$, Dash-dotted - $Q \approx 50$.

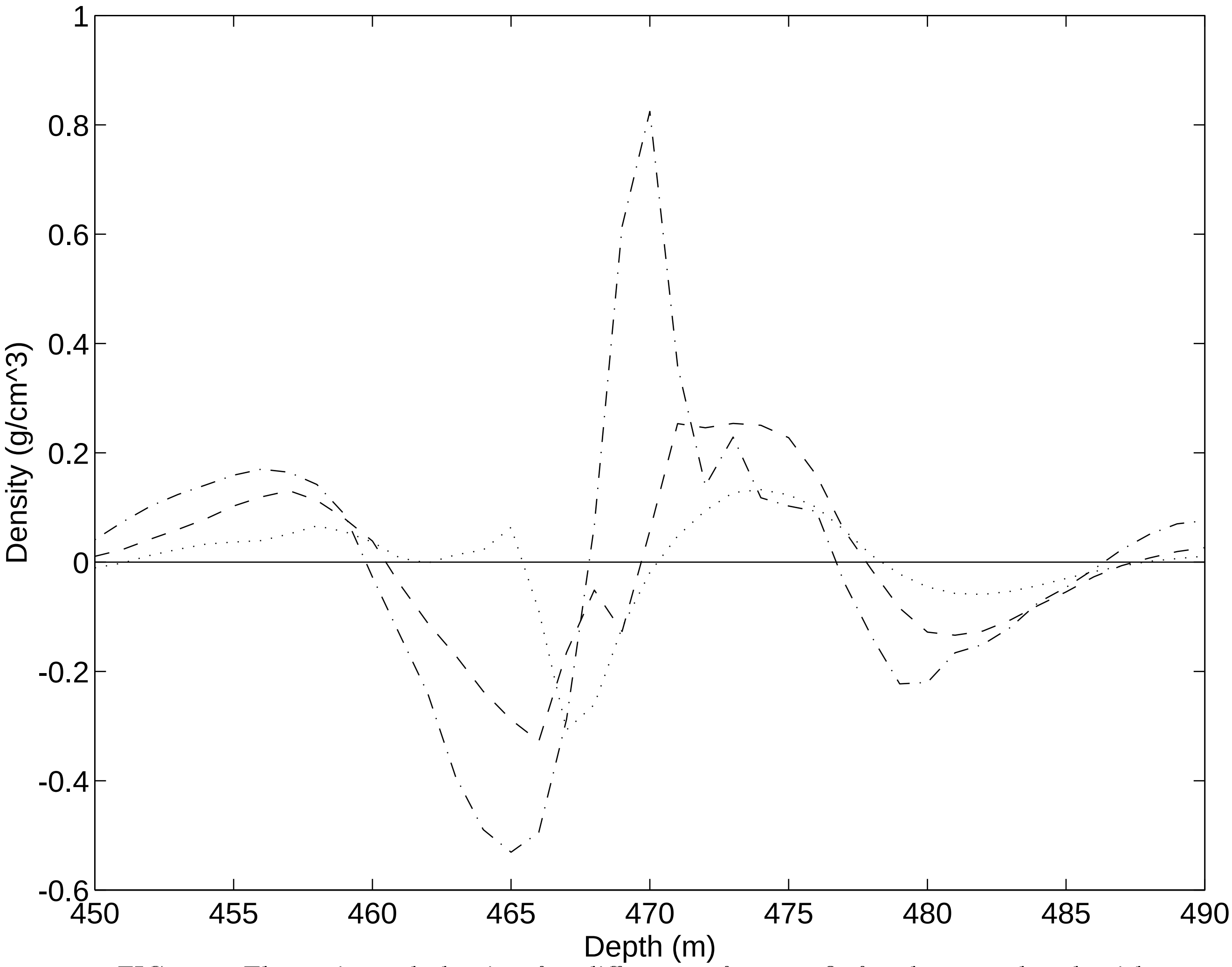

FIG. 23. The estimated density for different reference Q for data produced with $Q \approx 100$. Reflector 2. Solid - True reflector, Dashed - $Q \approx 100$, Dotted - $Q = \infty$, Dash-dotted - $Q \approx 50$.

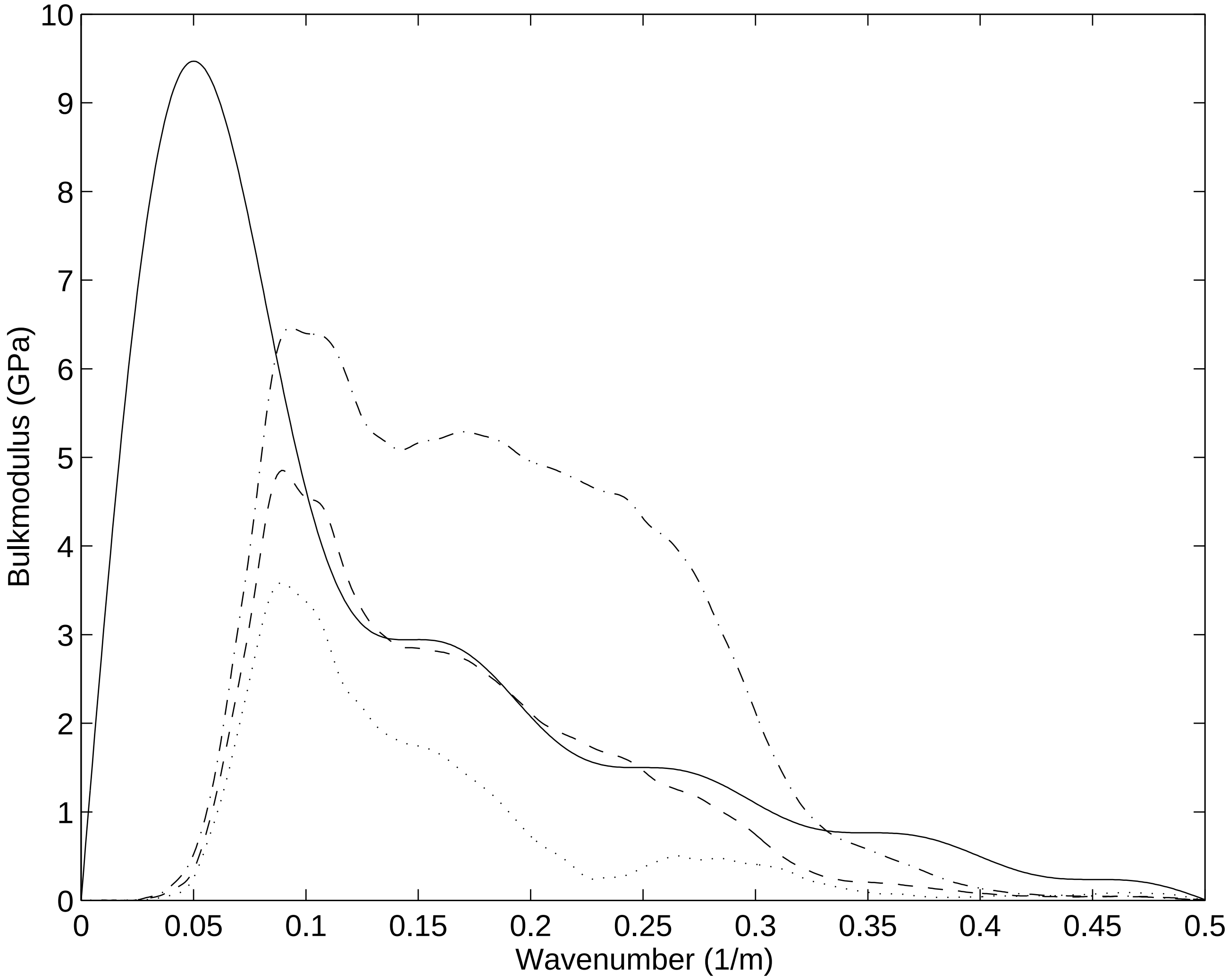

FIG. 24. Wavenumber spectrum of the estimated bulk modulus for different reference Q for data produced with $Q \approx 100$. Reflector 1. Solid - True reflector, Dashed - $Q \approx 100$, Dotted - $Q = \infty$, Dash-dotted - $Q \approx 50$.

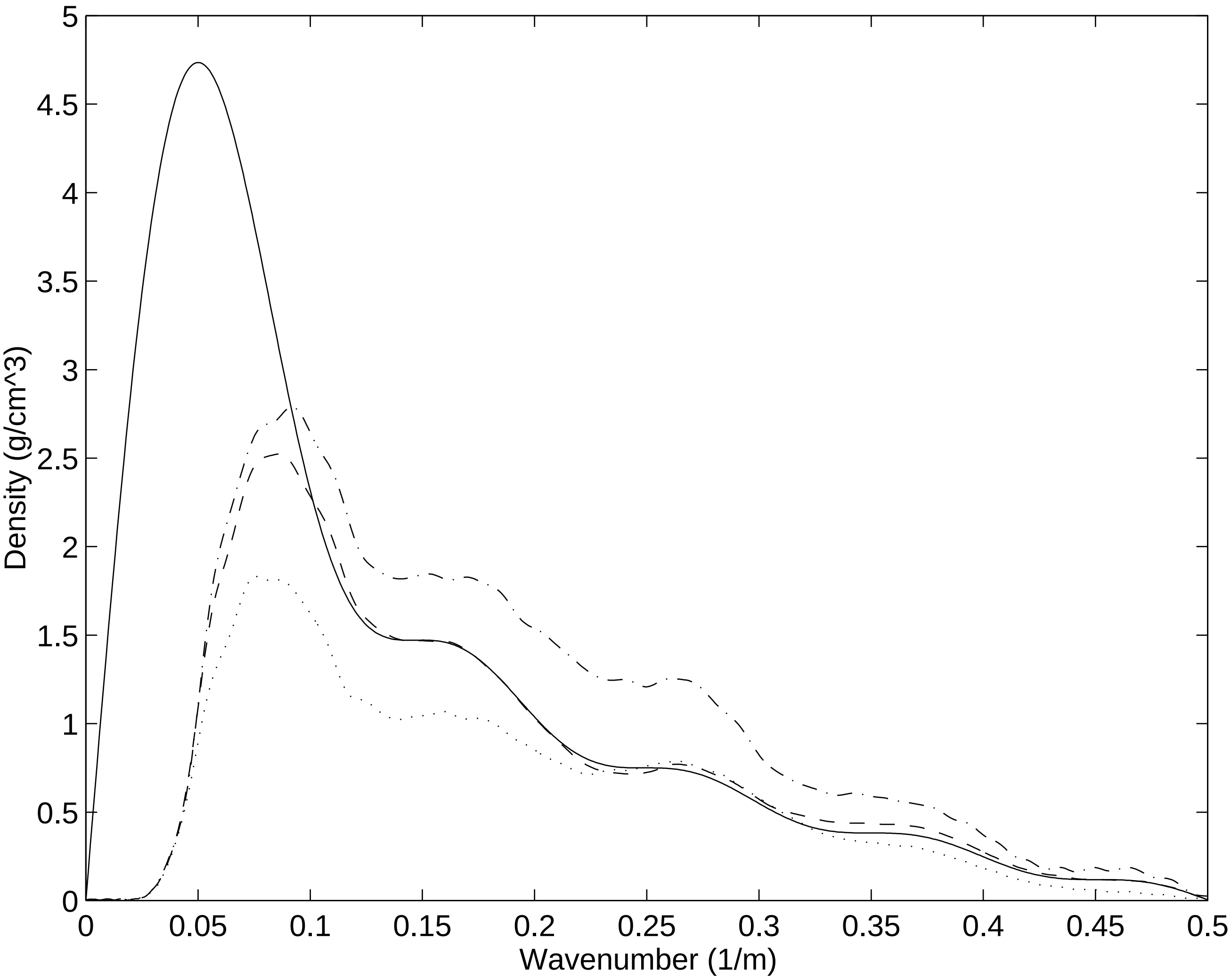

FIG. 25. Wavenumber spectrum of the estimated density for different reference Q for data produced with $Q \approx 100$. Reflector 1. Solid - True reflector, Dashed - $Q \approx 100$, Dotted - $Q = \infty$, Dash-dotted - $Q \approx 50$.

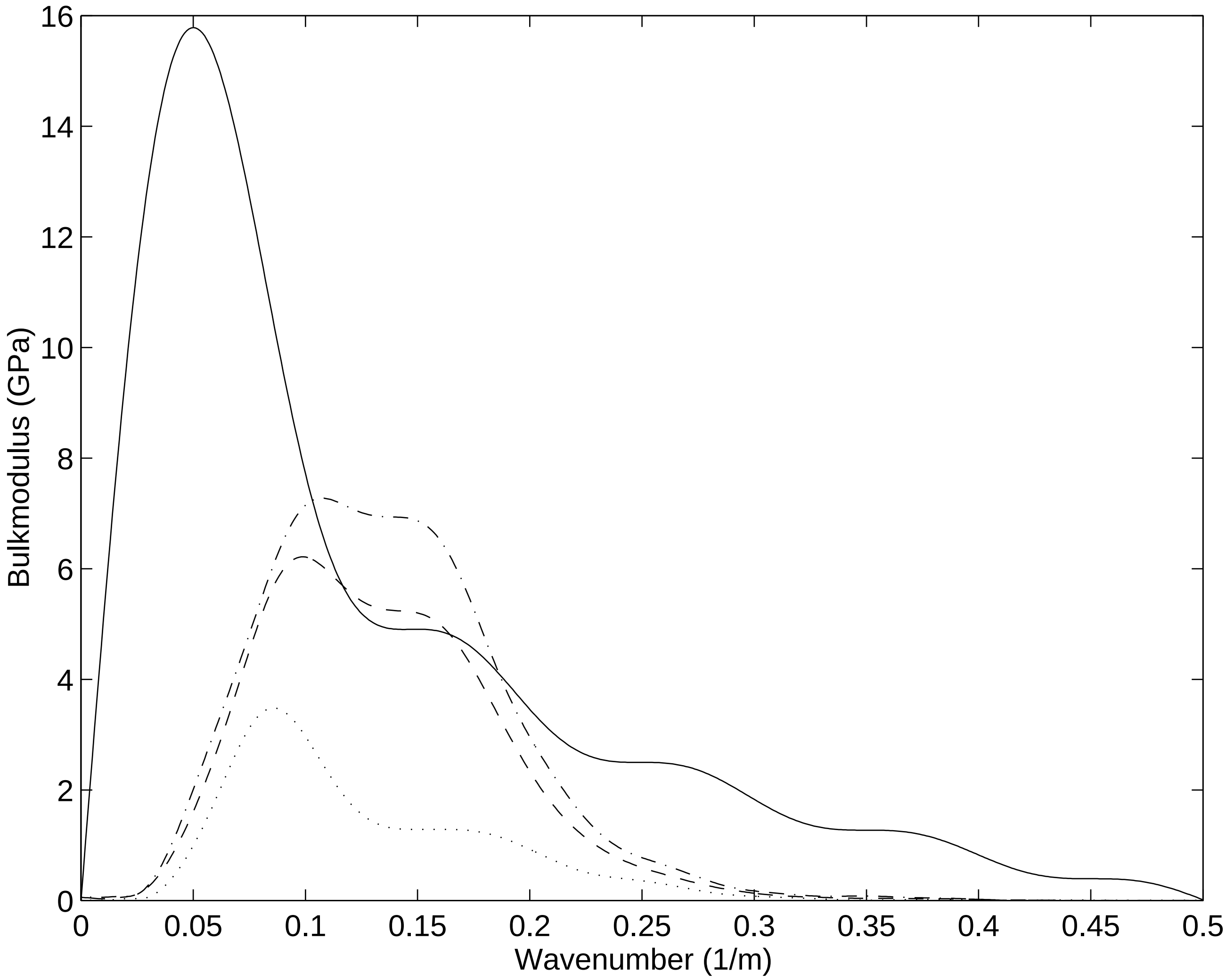

FIG. 26. Wavenumber spectrum of the estimated bulk modulus for different reference Q for data produced with $Q \approx 100$. Reflector 2. Solid - True reflector, Dashed - $Q \approx 100$, Dotted - $Q = \infty$, Dash-dotted - $Q \approx 50$.

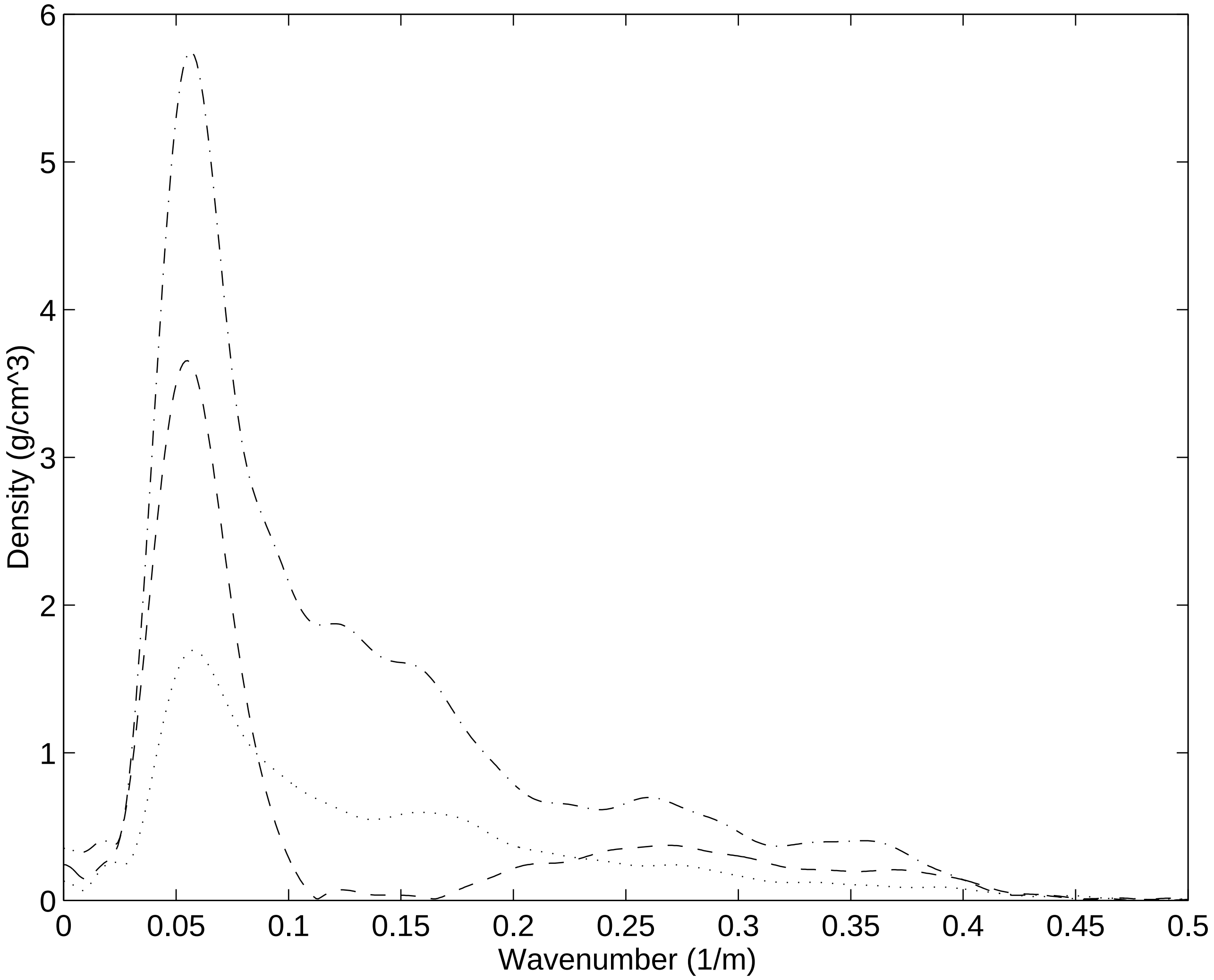

FIG. 27. Wavenumber spectrum of the estimated density for different reference Q for data produced with $Q \approx 100$. Reflector 2. Solid - True reflector, Dashed - $Q \approx 100$, Dotted - $Q = \infty$, Dash-dotted - $Q \approx 50$.

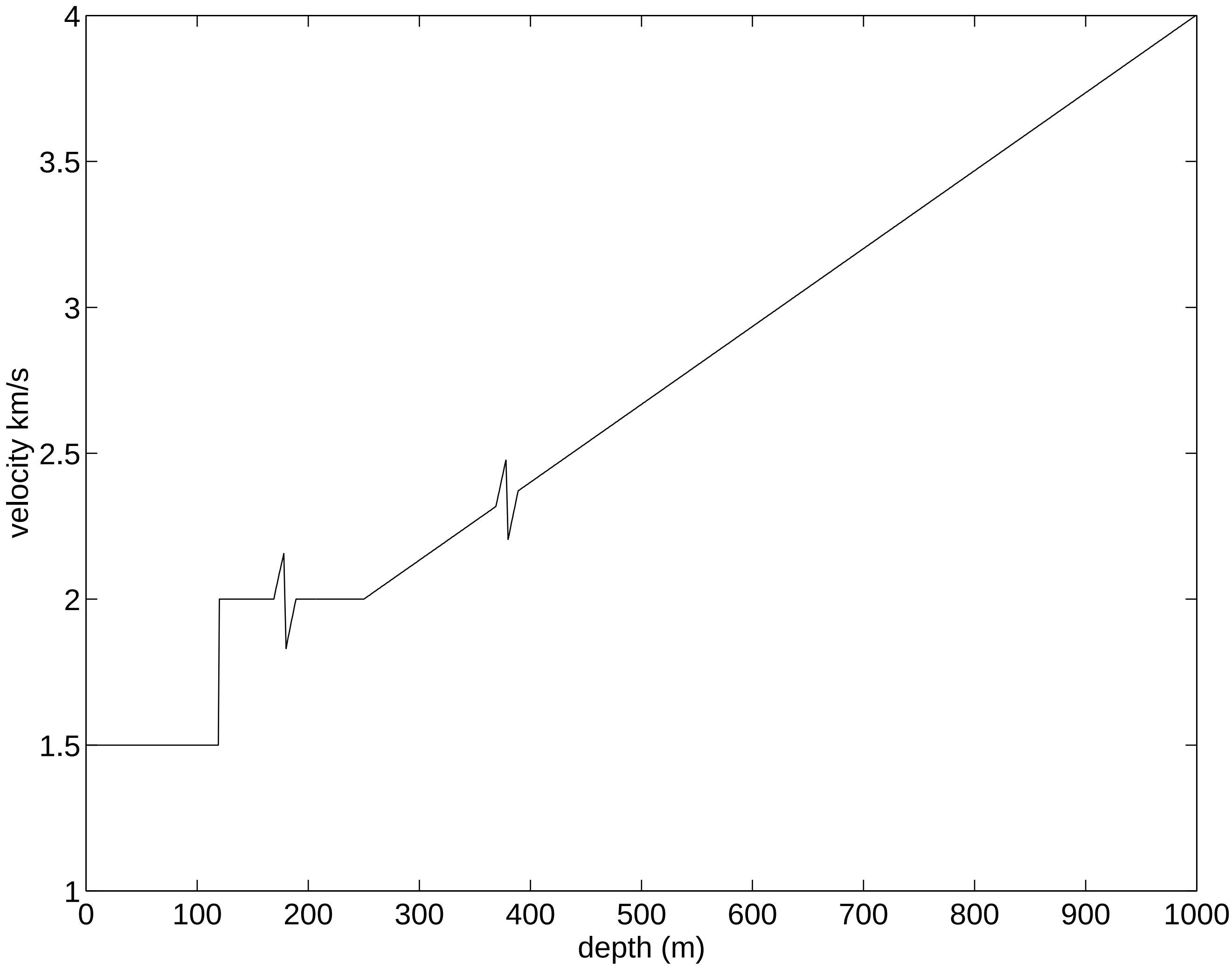

FIG. 28. Velocity model used to create synthetic data (non-linearized modeling).

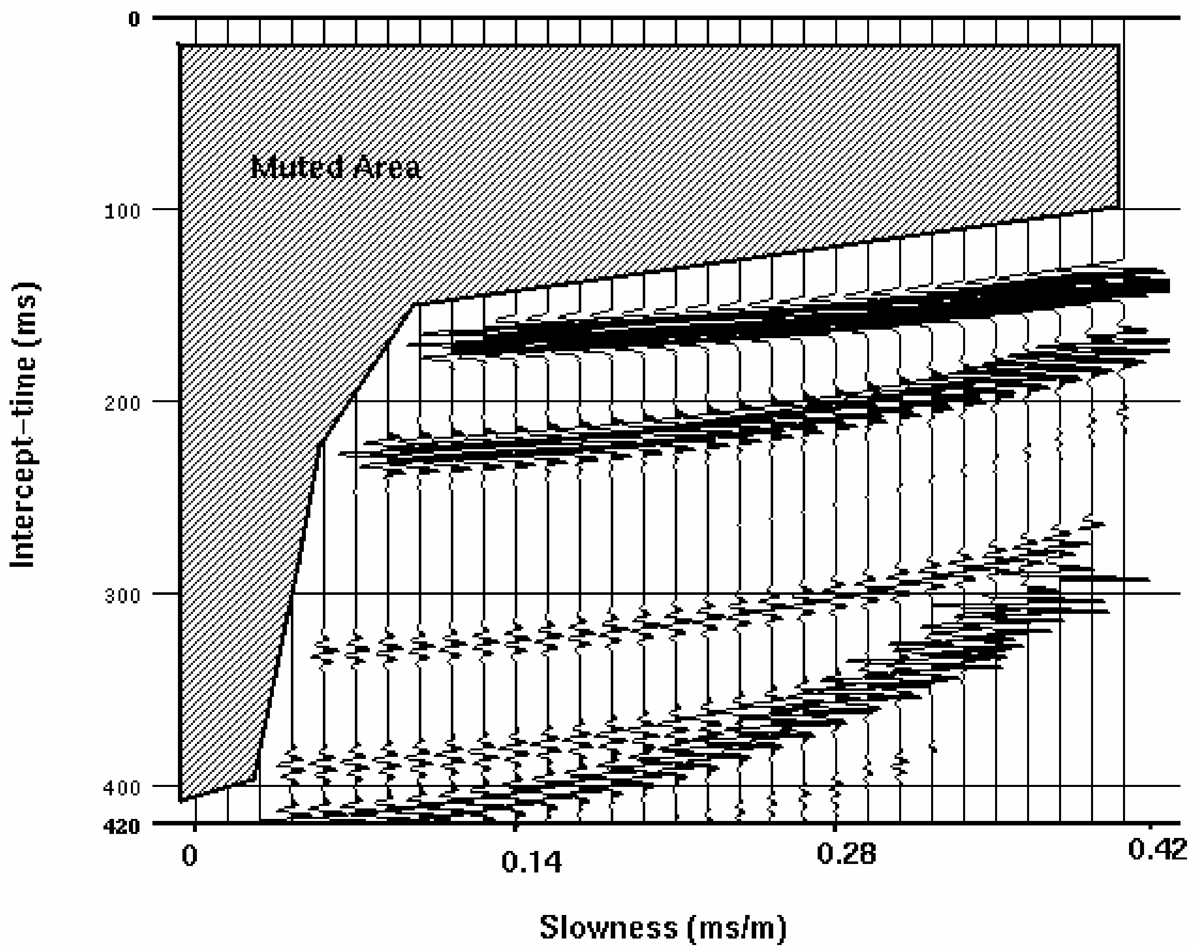

FIG. 29. Muted $\tau - p_s$ data from modeling. The direct wave is removed through muting. The data contains a clear water bottom multiple at 320 ms and a second multiple at 400 ms. The second multiple is created by a reflection from water bottom - water surface - first reflector.

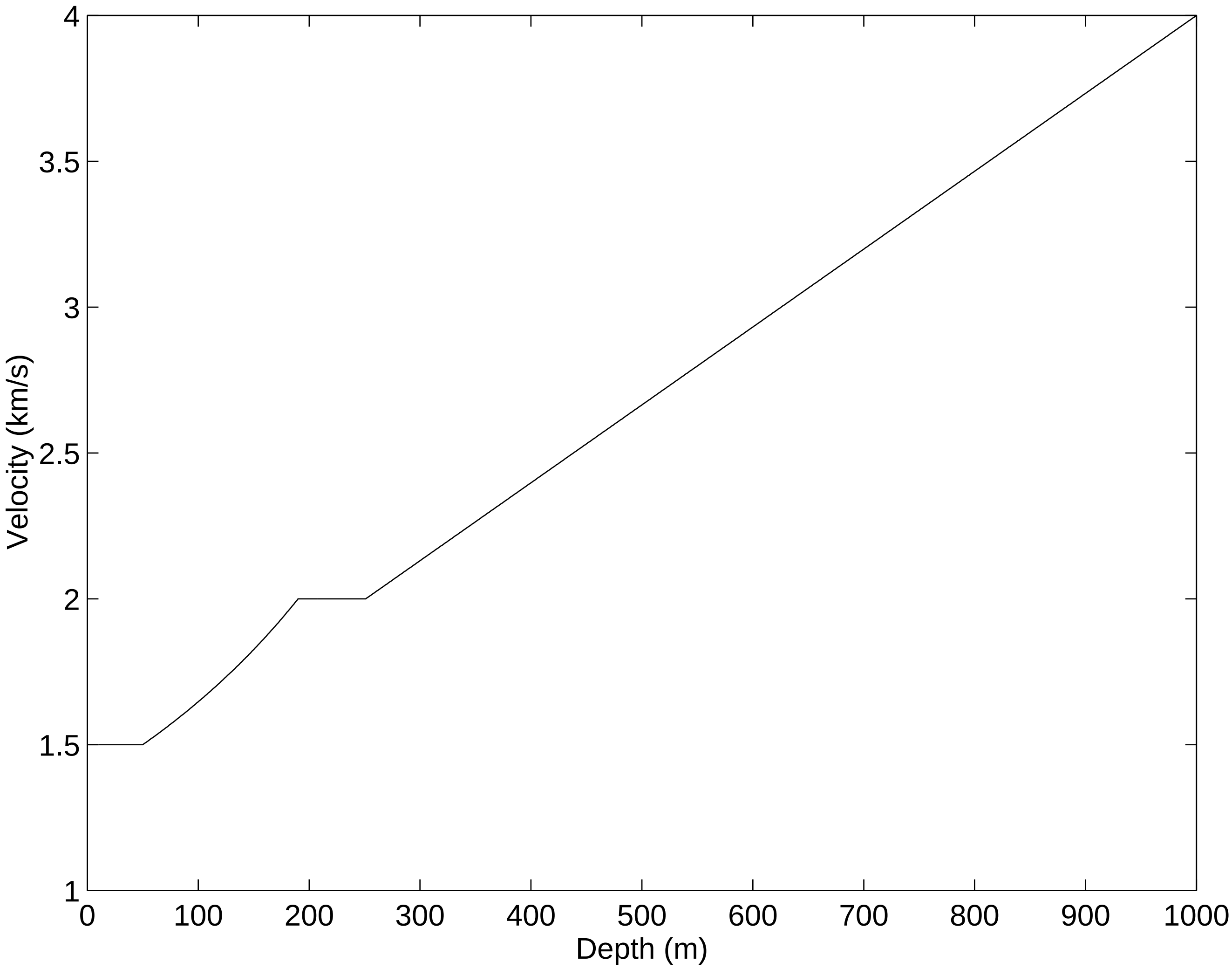

FIG. 30. The continuous background velocity used for the inversion.

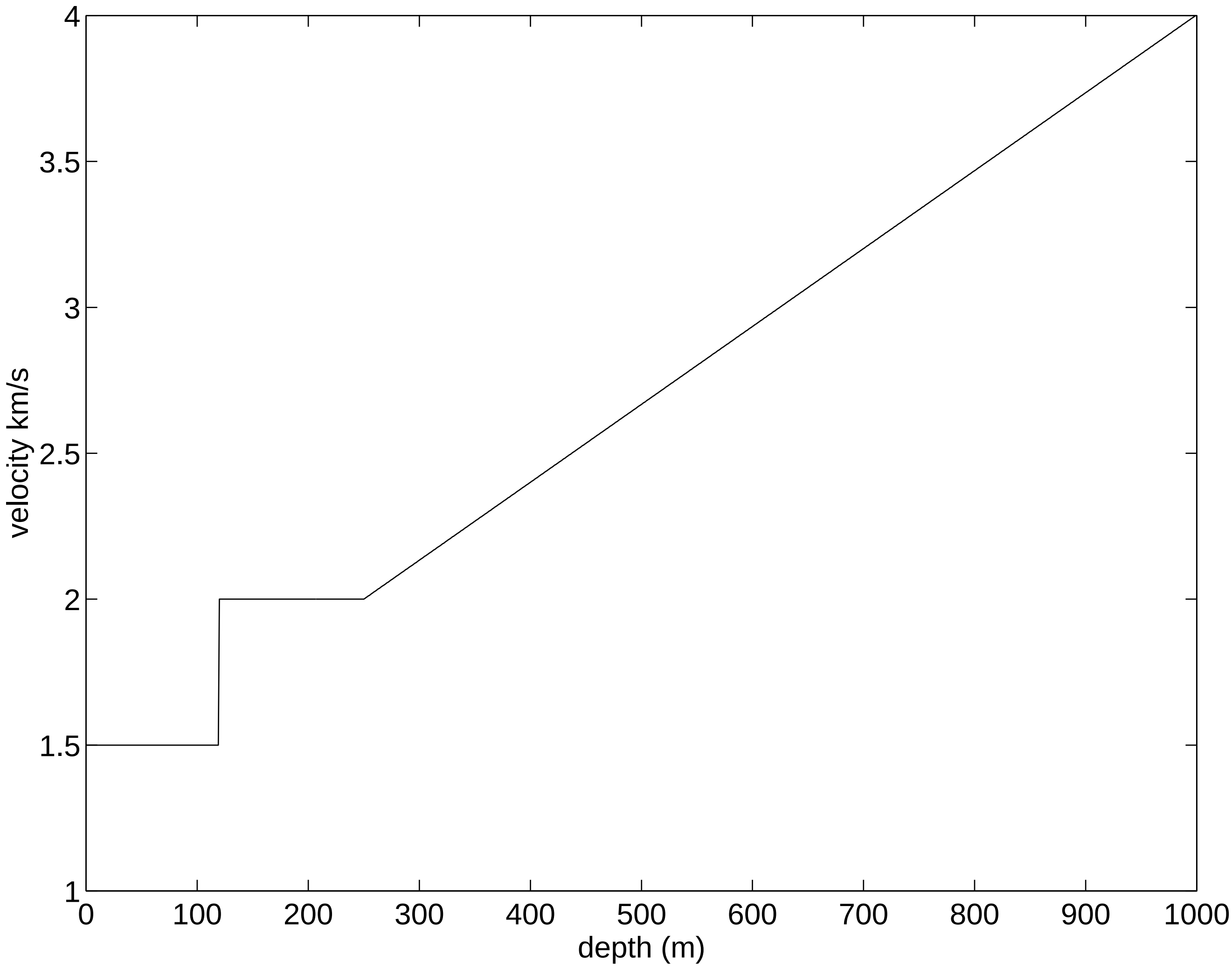

FIG. 31. The discontinuous background velocity used for the inversion.

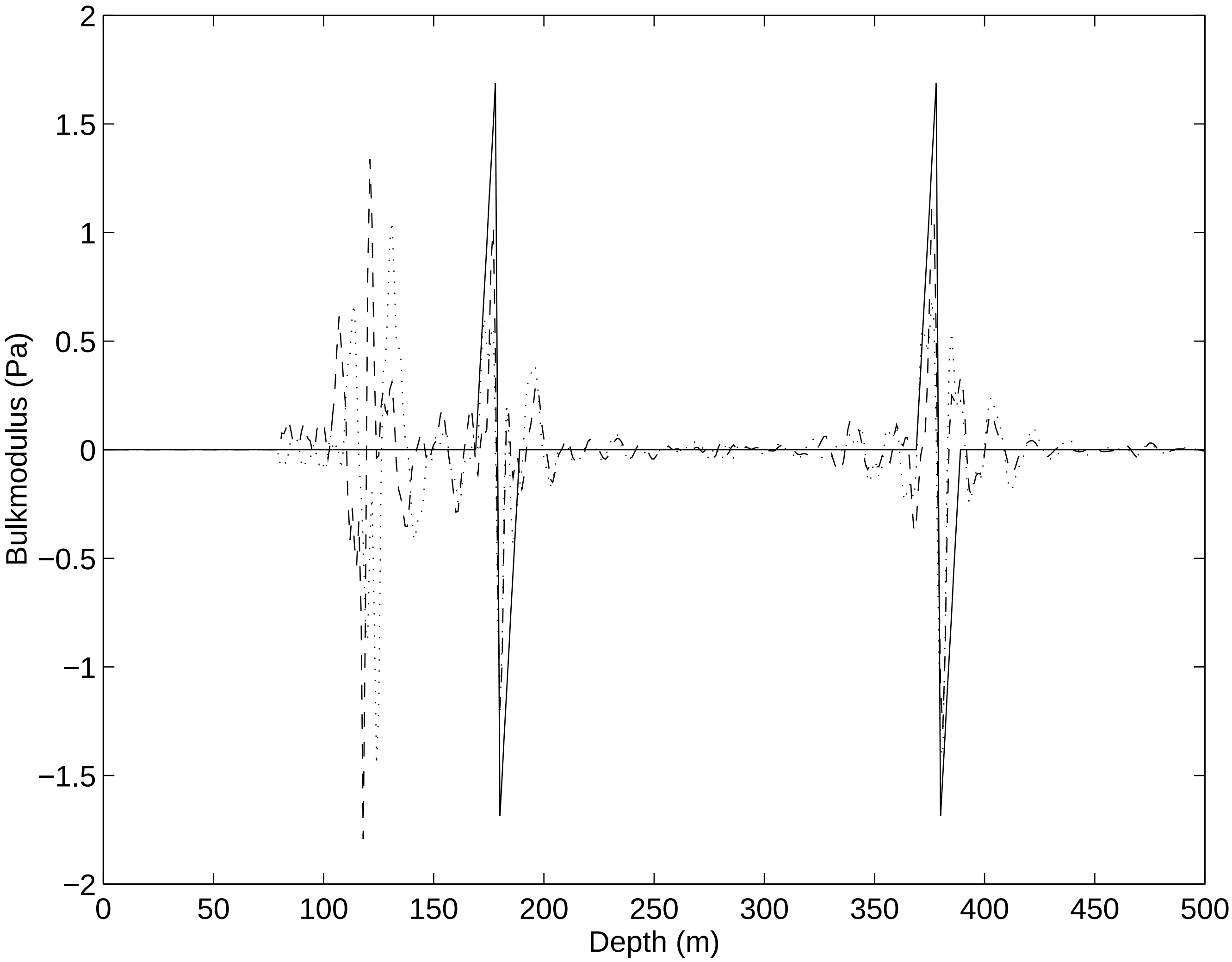

FIG. 32. True estimated bulk modulus for smooth and discontinuous velocity model. A range of 30 slowness values was used. No immediate indication can be found of the multiple. The solid line shows bulk modulus reflectivity representing the bumps in the velocity model in Figure 28, i.e., the true reflectivity and assumed linear part of the forward model. The dashed line is the estimated result, when the discontinuous background model (Figure 31) was used. The dotted line is the estimated result, when the smooth background model (Figure 30) was used.

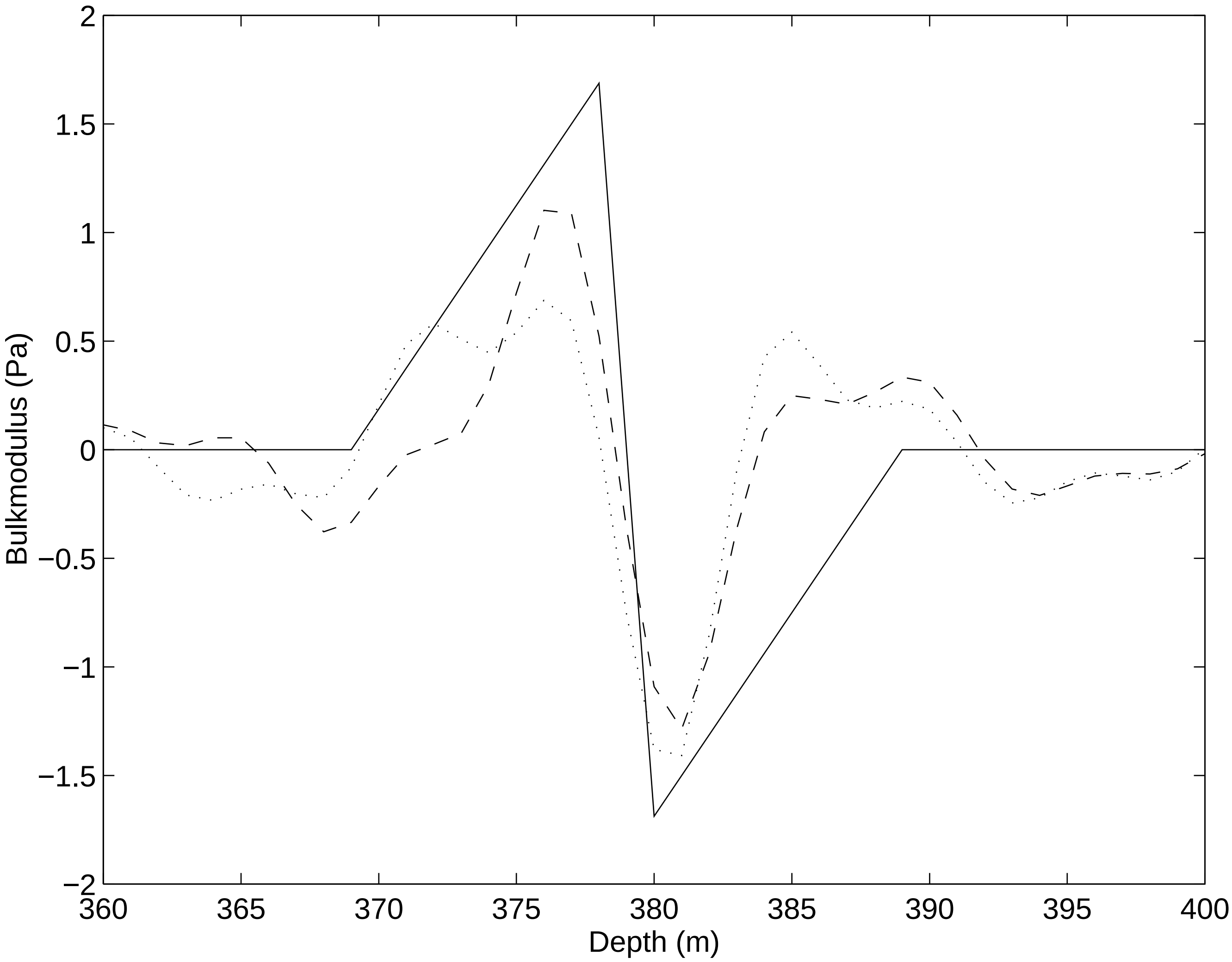

FIG. 33. True estimated bulk modulus for smooth and discontinuous velocity model. A range of 30 slowness values was used. A close-up of the deepest reflector. The reflector estimated with the smooth velocity model seems to be a slightly worse estimated of the true reflector than the estimate obtained with the discontinuous velocity model. The solid line shows bulk modulus reflectivity representing the bumps in the velocity model in Figure 28, i.e., the true reflectivity and assumed linear part of the forward model. The dashed line is the estimated result, when the discontinuous background model (Figure 31) was used. The dotted line is the estimated result, when the smooth background model (Figure 30) was used.

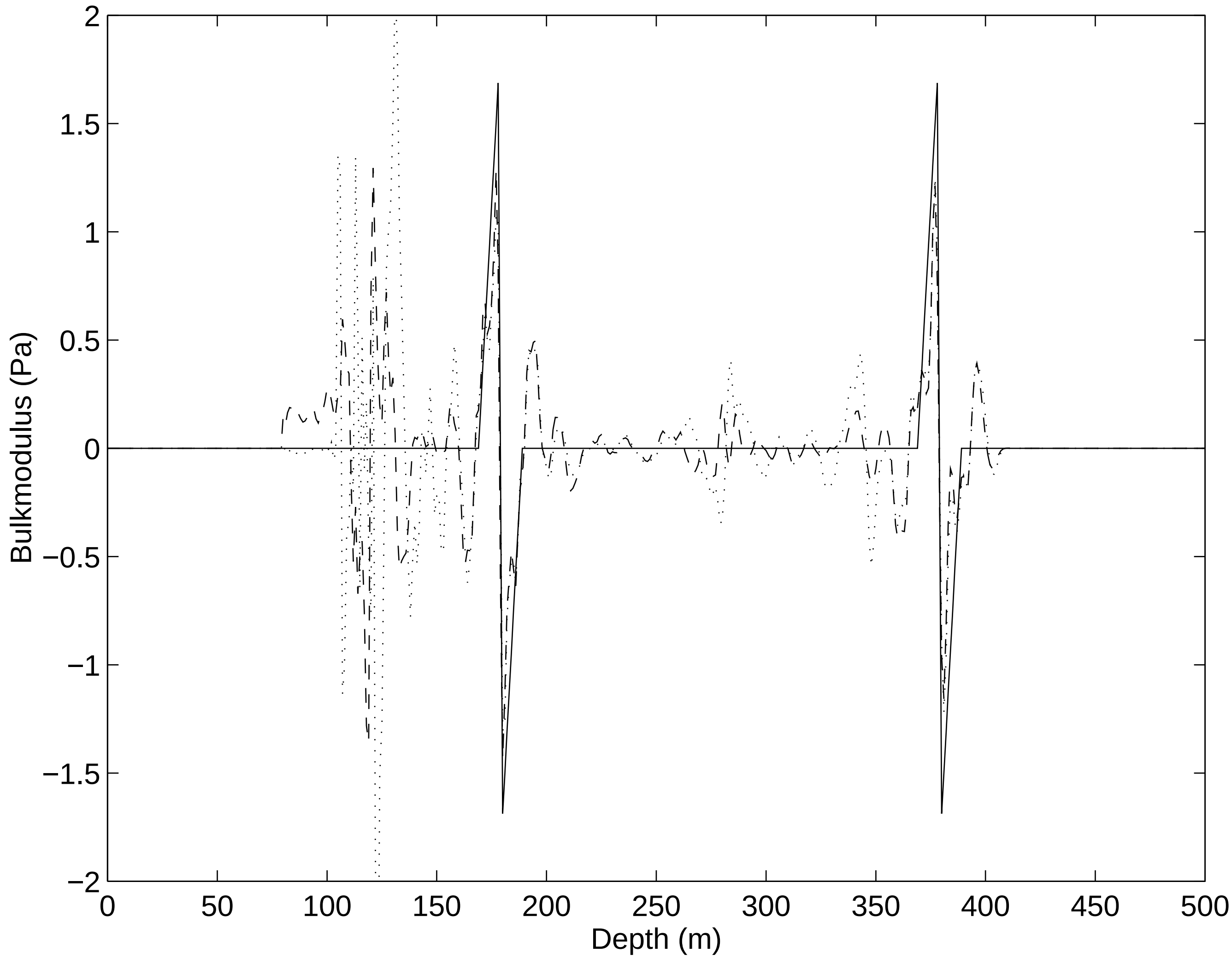

FIG. 34. True estimated bulk modulus for smooth and discontinuous velocity model. A range of 10 slowness values was used. The estimate obtained using the smooth velocity model show two false reflectors between the two true reflectors. The false reflectors are clearly caused by the multiple energy. The solid line shows bulk modulus reflectivity representing the bumps in the velocity model in Figure 28, i.e., the true reflectivity and assumed linear part of the forward model. The dashed line is the estimated result, when the discontinuous background model (Figure 31) was used. The dotted line is the estimated result, when the smooth background model (Figure 30) was used.

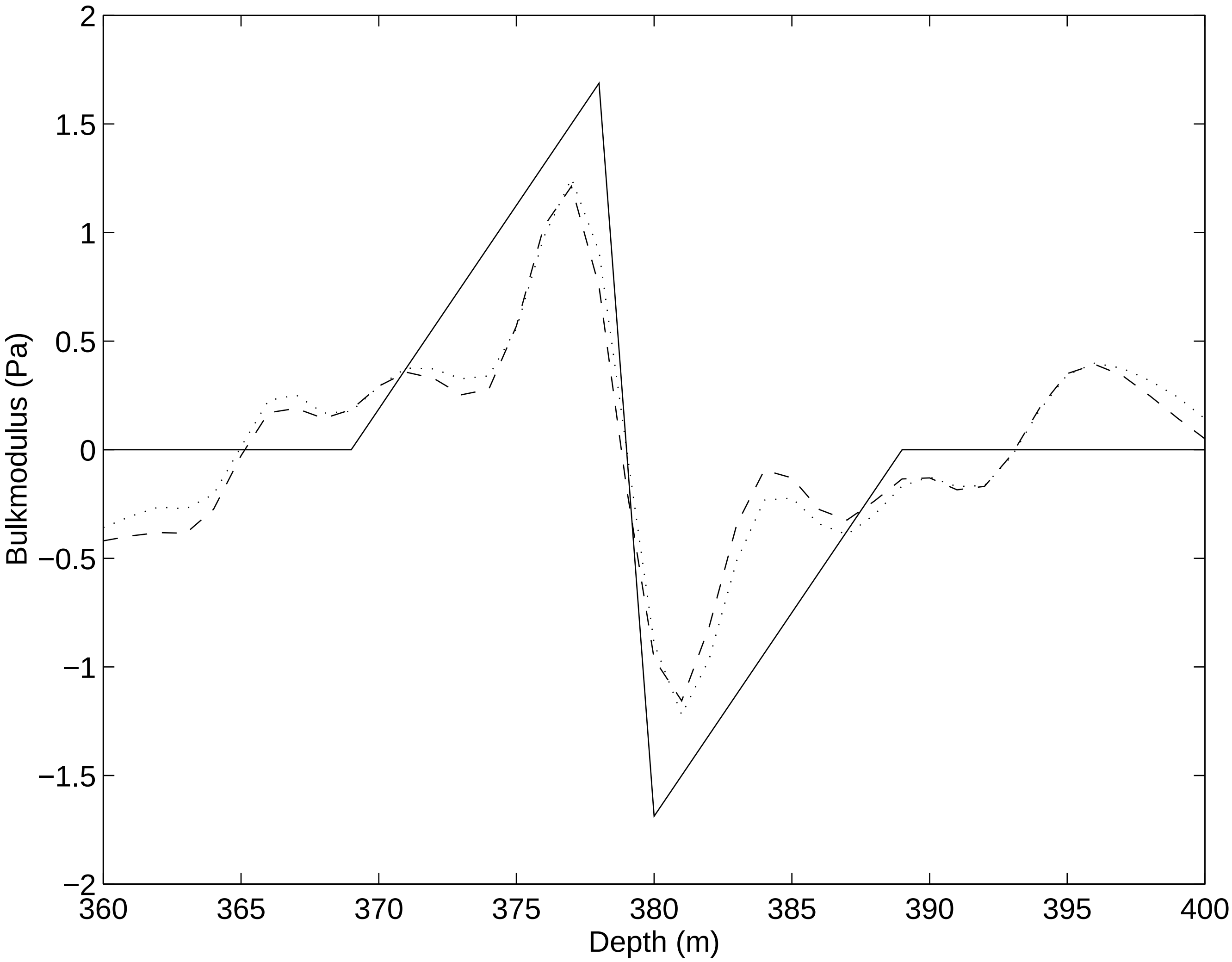

FIG. 35. True estimated bulk modulus for smooth and discontinuous velocity model. A range of 10 slowness values was used. A close-up of the deepest reflector. The estimates of the deepest reflector are essentially identical for both velocity models. The solid line shows bulk modulus reflectivity representing the bumps in the velocity model in Figure 28, i.e., the true reflectivity and assumed linear part of the forward model. The dashed line is the estimated result, when the discontinuous background model (Figure 31) was used. The dotted line is the estimated result, when the smooth background model (Figure 30) was used.

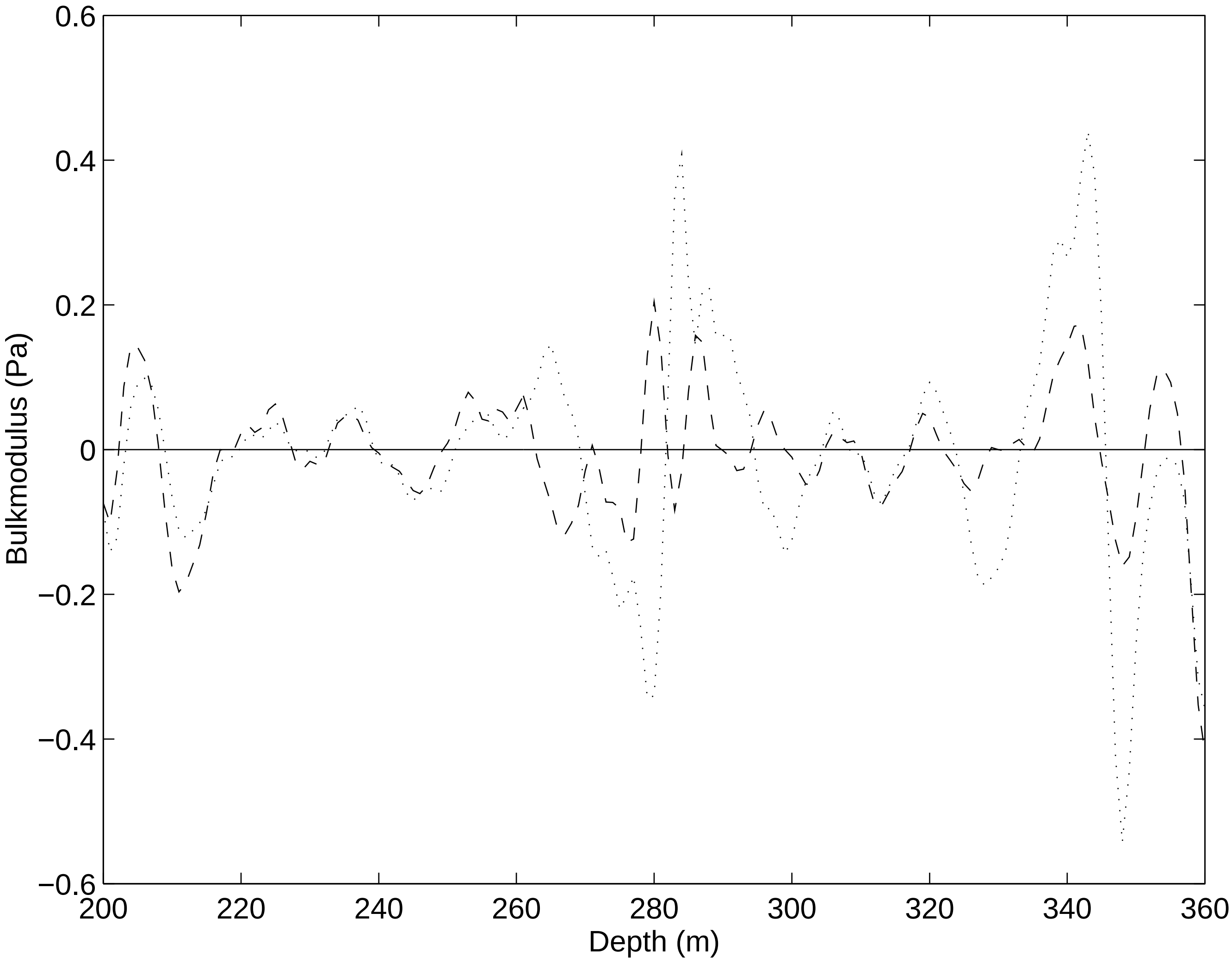

FIG. 36. True estimated bulk modulus for smooth and discontinuous velocity model. A range of 10 slowness values was used. A close-up of the deepest reflector. The estimates of the deepest reflector are essentially identical for both velocity models. The solid line shows bulk modulus reflectivity representing the bumps in the velocity model in Figure 28, i.e., the true reflectivity and assumed linear part of the forward model. The dashed line is the estimated result, when the discontinuous background model (Figure 31) was used. The dotted line is the estimated result, when the smooth background model (Figure 30) was used.